SCIENCE CHINA
Chemistry

•REVIEWS•

https://doi.org/10.1007/s11426-024-2212-0

Active sites and reaction mechanisms of CO_x hydrogenation on zinc-based mixed oxide catalysts

Zhuo-Yan Yao[1], Sicong Ma[2*] & Zhi-Pan Liu[1,2,3*]

[1]*Shanghai Key Laboratory of Molecular Catalysis and Innovative Materials, Key Laboratory of Computational Physical Science, Department of Chemistry, Fudan University, Shanghai 200433, China;*
[2]*State Key Laboratory of Metal Organic Chemistry, Shanghai Institute of Organic Chemistry, Chinese Academy of Sciences, Shanghai 200032, China;*
[3]*Shanghai Qi Zhi Institution, Shanghai 200030, China*

Received June 6, 2024; accepted July 17, 2024; published online September 9, 2024

The conversion of C1 molecules, CO_x (CO and CO_2), to valuable chemical products has garnered ever-increasing attention. Among many routes, the hydrogenation via thermal catalysis is particularly promising as a key clean energy technology with the increasing supply of green H_2. Zinc-based mixed oxide catalysts exhibit exceptional catalytic performance in the CO_x hydrogenation to value-added hydrocarbons, especially in combination with zeolite. This review overviews the recent achievements in understanding the active sites and reaction mechanisms of CO_x hydrogenation on zinc-based mixed oxide catalysts, focusing on three most-studied zinc-based mixed oxide catalysts, namely $ZnCrO_x$, $ZnAlO_x$ and $ZnZrO_x$. The challenges and future directions are also discussed.

Zn-based oxide, CO_x hydrogenation, active site, reaction mechanism

Citation: Yao ZY, Ma S, Liu ZP. Active sites and reaction mechanisms of CO_x hydrogenation on zinc-based mixed oxide catalysts. *Sci China Chem*, 2024, 67, https://doi.org/10.1007/s11426-024-2212-0

1 Introduction

C1 chemistry represents a pivotal and attractive research domain in chemistry and catalysis, driven by the increasing demand for producing value-added chemicals and fuels from alternative sources [1–7]. Among various pathways, CO_x (CO and CO_2) hydrogenation emerges as the most crucial reactions for utilizing clean energy technologies [8–17]. Recent years have seen a growing interest in the utilization of metal oxide-zeolite (OX-ZEO) bifunctional catalysts for the direct synthesis of C_{2+} product from CO_x hydrogenation under high temperature conditions [8]. The catalytic activity of the reaction is primarily determined by the metal oxides that work for CO_x/H_2 adsorption and activation. It was found that Zn-based mixed oxide, i.e., $ZnCrO_x$ [8,18], $ZnAlO_x$ [19], $ZnGaO_x$ [18] and $ZnZrO_x$ [20], are among the best catalysts, showing excellent activity and stability. These mixed oxide catalysts can be coupled with the zeolites to facilitate CO_x hydrogenation to generate various products, including hydrocarbons, dimethyl ether (DME), formic acid, and ethanol [8,10,12,18,20–25].

Zinc oxide is known for its strong dissociation ability for H_2 but relatively poor activation ability for CO_x. By combining zinc oxide with many other elements such as Cr, Zr, Al, and Mn, the key surface properties, including surface oxygen vacancy (O_V) content, H_2 dissociation ability, and CO_x affinity can be regulated, enabling the synergistic activation of CO_x and H_2, thereby enhancing the activity of CO_x hydrogenation reactions. For instance, $ZnCrO_x$ catalyst has been a well-established catalyst for syngas-to-methanol since

Published in virtual special issue "Advanced theory-guided catalysis"
*Corresponding authors (email: scma@mail.sioc.ac.cn; zpliu@fudan.edu.cn)

1930s [26]; ZnO-ZrO_2 was reported to efficiently reduce CO_2 to methanol [13,27]; Cu/ZnO/Al_2O_3, the well-known industrial catalyst, achieves low-pressure and low-temperature hydrogenation of CO_x mixed gas to methanol [28–30]. The resulting methanol serves as a crucial feedstock for subsequent catalytic conversions.

Since 1970s, zeolites have been established as prominent catalysts for methanol conversion. The product selectivity varies with different zeolite topologies, ranging from gasolines [31,32], light olefins [33,34] to aromatics [35,36] etc. Despite the high methanol conversion rate using zeolite catalysts, the processes like methanol-to-olefin, methanol-to-gasoline, and methanol-to-aromatics all experience the rapid deactivation [32,35–40]. For example, the methanol-to-gasoline process with modified ZSM-5 zeolites typically achieves >85% high methanol conversion and gasoline selectivity, but is prone to quick deactivation due to coke formation.

In contrast to the separate route that uses methanol as a platform molecule, the OX-ZEO bifunctional catalysts can directly convert CO_x/H_2 feeds into selected hydrocarbon product mixtures in a single reactor. This process involves the oxide component converting syngas or CO_2/H_2 to oxygenates (such as methanol, DME, or ketene), and the zeolite component subsequently converting these oxygenates to hydrocarbons. The OX-ZEO route thus offers new opportunities to overcome thermodynamic limitations and to intensify chemical processes by reducing the number of separation steps and product workup. Especially, CO_x/H_2 would also be present in the zeolite that helps to inhibit the coke formation and avoid the deactivation. However, many challenges still remain, including the finding of optimum reaction conditions, the search for the best catalytic performance and the identification of the reaction intermediates. For the reaction intermediate, for example, Bao and co-workers [8] based on the experiments on a bifunctional catalyst consisting of Zn-Cr oxide and mesoporous SAPO-34 propose that the OX-ZEO process operates via ketene as the key intermediate. But, Wang and co-workers [41] suggested methanol and DME as reaction intermediates on their bifunctional catalysts comprising Zr-Zn oxides and SAPO-34 as active components for CO activation and C–C coupling step. In both cases, SAPO-34 was used to convert oxygenates to lower olefins, but the different Zn-based oxides appear to yield different reaction intermediates, indicating the importance of OX types in OX-ZEO catalysts in determining the catalytic activity and the nature of the reaction intermediates.

To further illustrate the influence of Zn-based oxides, Figure 1, Tables 1 and 2 summarize the CO_x conversion rate versus product selectivity on three typical Zn-based OX-ZEO catalysts from experiments, where OXs are $ZnCrO_x$, $ZnAlO_x$ and $ZnZrO_x$, represented by black points, orange triangles and blue squares, respectively. These experimental results are briefly introduced in the following.

$ZnCrO_x$|MSAPO-34 catalyst was the first OX-ZEO catalyst reported by Bao and co-workers [8] in 2016 for syngas-to-olefin (STO). The initial CO conversion rate for STO

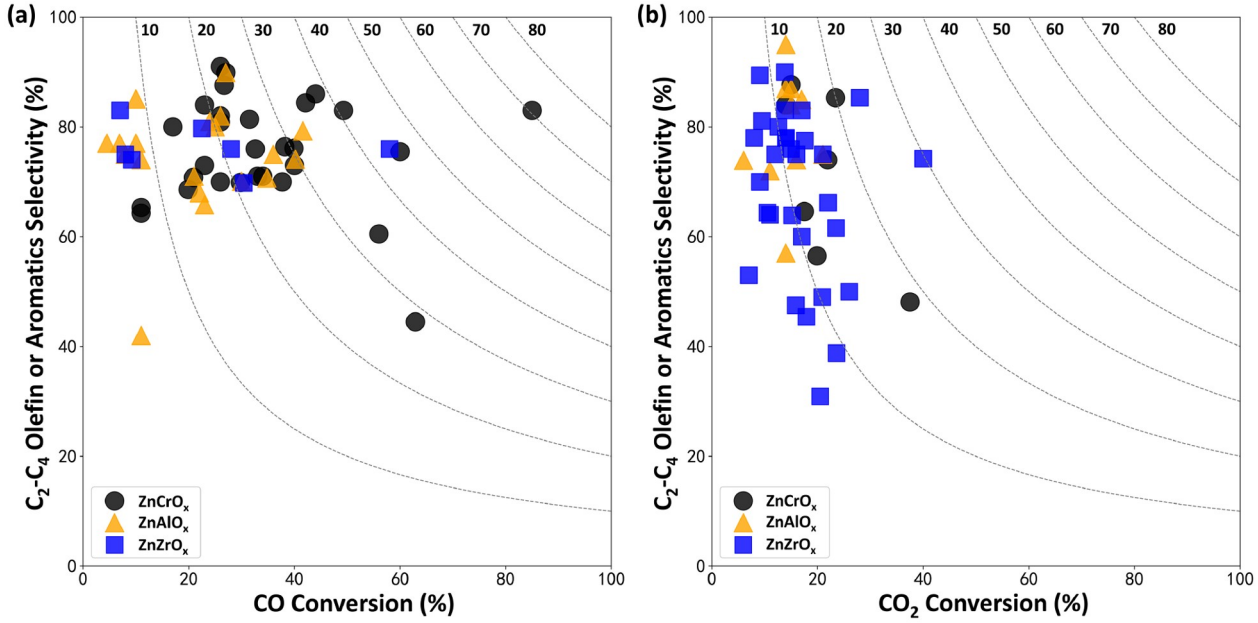

Figure 1 (Color online) Selectivity of light olefin or aromatics in hydrocarbons versus conversion data on CO (a) and CO_2 (b) hydrogenation with Zn-based OX-ZEO catalysts (all data from experiments in Tables 1 and 2). $ZnCrO_x$, $ZnAlO_x$ and $ZnZrO_x$ are depicted as black points, orange triangles and blue squares respectively. The product yields (CO_x conversion rate times product selectivity) are plotted in gray dashed lines. Note that the selectivity reported in experiments does not take into account of CO_2 production in CO hydrogenation and CO production in CO_2 hydrogenation.

Table 1 Zn-based OX-ZEO bifunctional catalysts reported for CO hydrogenation to various hydrocarbons and their performance[a]

Oxide	Zeolite	T (K)	P (MPa)	GHSV	H_2/CO	X_{CO}	S_{CO_2}	S_{CH_4}	$S_{C_2^=-C_4^=}$	$S_{C_2-C_4}$	$S_{C_{5+}}$	$S_{Arom.}$	Ref.
$ZnCrO_x$	MSAPO-34	673	2.5	7714	2.5	17.0	44.0	2.0	80.0	93.0	5.0	–	[8]
$ZnAl_2O_4$	SAPO-34	673	3	3600	2.0	25.0	44.0	3.5	80.0	94.0	2.4	–	[18]
$ZnAlO_x$	SAPO-34	663	4	12000	1.0	6.9	33.1	5.5	77.0	91.0	3.0	–	[19]
Zn-ZrO_2	SSZ-13	673	3	3000	2.0	28.0	42.0	2.0	76.0	96.0	2.0	–	[20]
$ZnCrO_x$	MOR-py	633	2.5	1857	2.5	26.0	48.0	1.0	91.0	95.0	5.0	–	[24]
ZnO-ZrO_2	SAPO-34	673	1	3600	2.0	9.2	45.0	5.0	74.0	91.0	4.0	–	[41]
ZnCr alloy	DAY	623	2.1	6588	2.0	11.0	47.2	7.0	–	65.3	27.8	0.0	[42]
$ZnCrO_x$	GeAPO-18	703	6	1500	2.5	85.0	32.0	2.0	83.0	92.0	7.0	–	[43]
$ZnCrO_x$ as core	SAPO-34 as shell	673	2	6480	2.0	11.0	36.2	8.0	64.3	25.0	3.0	–	[46]
$ZnCrO_x$	SAPO-34	673	2	5400	2.0	26.0	44.4	4.0	80.9	89.0	7.0	–	[47]
$ZnCrO_x$	SAPO-34	673	4	5400	2.0	39.9	44.3	3.0	76.1	87.5	9.5	–	[47]
$ZnCrO_x$	SAPO-34	673	4	5400	2.0	42.1	57.6	1.7	84.4	90.5	7.8	–	[48]
$ZnCrAlO_x$	SAPO-34	648	1	3000	2.0	26.0	46.0	2.0	82.0	92.0	6.0	–	[49]
$ZnCrO_x$	SAPO-34	673	4	5000	2.5	60.0	38.7	3.1	75.5	93.0	3.9	–	[50]
ZnO-$ZnCr_2O_4$	SAPO-34	673	1	3600	2.0	34.0	48.0	13.0	71.0	87.0	0.0	–	[51]
$ZnCrO_x$	H-SSZ-13	653	1	6000	2.0	20.9	48.0	6.0	70.8	87.7	6.3	–	[52]
$ZnCrO_x$	AlPO-18	663	10	3600	1.0	49.3	49.0	2.0	83.0	87.0	11.0	–	[53]
$ZnCrO_x$	SAPO-18	653	1	6000	2.0	19.9	49.2	2.3	68.6	84.8	12.9	–	[54]
$ZnCrO_x$	SAPO-17	673	4	1800	1.0	38.2	47.6	1.8	76.4	82.5	4.8	–	[55]
$ZnCrO_x$ HoMS	H-MCM-22	673	2	12000	2.5	23.0	40.0	7.0	84.0	89.0	2.0	–	[56]
$ZnCrO_x$	SAPO-18/34 intergrowths	663	4	1200	1.0	26.7	46.5	1.3	87.6	89.8	8.1	–	[58]
$ZnCrO_x$	SAPO-18/34 intergrowths	663	4	1200	1.0	31.5	46.5	2.0	81.4	90.3	7.5	–	[58]
$ZnAl_2O_4$	MOR	643	3	1500	1.0	10.0	44.0	5.0	77.0	12.0	6.0	–	[59]
ZnO-Cr_2O_3	ZSM-5	700	8.3	1780	–	37.7	50.0	2.5	–	25.9	72.0	70.0	[63]
ZnO-Cr_2O_3	ZSM-5	673	4	360	0.5	62.9	70.5	3.7	–	40.7	55.6	44.5	[64]
Fe-$ZnCr_2O_4$	H-ZSM-5	653	4	1500	1.0	40.0	48.0	4.0	3.0	17.0	81.0	73.0	[66]
$ZnCrO_x$	H-ZSM-5	623	4	3000	1.0	26.0	35.0	1.0	9.0	15.0	84.0	70.0	[67]
$ZnCr_2O_4$	H-ZSM-5	663	3	1500	1.0	32.6	46.9	2.1	2.9	15.1	82.8	76.0	[68]
ZnO-$ZnCr_2O_4$	ZSM-5	623	4	3000	1.0	23.0	31.0	2.0	6.0	14.0	85.0	73.0	[69]
$ZnCrO_x$	ZSM-5	623	4	3000	1.0	29.8	34.8	0.5	6.0	14.9	84.5	69.9	[70]
Zn-Al_2O_3	SAPO-34	673	1	3600	2.0	4.5	46.1	10.4	77.0	89.6	5.9	–	[78]
$ZnAlO_x$	BAI-CHA	623	1	2400	2.0	10.0	43.0	4.0	85.1	94.0	2.0	–	[79]
$ZnAlO_x$	SAPO-34	673	3	3000	2.0	24.0	45.0	3.7	81.0	95.0	1.4	–	[80]
$ZnAlO_x$	SAPO-35	673	3	3000	2.0	11.0	41.0	42.0	11.3	33.4	4.6	–	[80]
$ZnAlO_x$	SAPO-17	673	3	3000	2.0	23.0	42.0	13.0	65.8	80.2	6.8	–	[80]
$ZnAlO_x$	SAPO-18	673	3	3000	2.0	21.0	44.0	2.9	71.0	87.3	10.0	–	[80]
$ZnAlO_x$	SAPO-11	623	3	3000	2.0	36.0	44.0	2.4	14.7	22.3	75.0	–	[80]
$ZnAlO_x$	SAPO-31	623	3	3000	2.0	22.0	40.0	1.3	24.6	27.1	68.0	–	[80]
$ZnAlO_x$	SAPO-5	673	3	3000	2.0	30.0	41.0	7.9	13.7	70.1	22.0	–	[80]
$ZnAlO_x$	HY	673	3	3000	2.0	11.0	39.0	8.9	13.0	74.0	17.0	–	[80]

(*To be continued on the next page*)

(*Continued*)

Oxide	Zeolite	T (K)	P (MPa)	GHSV	H_2/CO	X_{CO}	S_{CO_2}	S_{CH_4}	$S_{C_2^=-C_4^=}$	$S_{C_2-C_4}$	$S_{C_{5+}}$	$S_{Arom.}$	Ref.
$ZnAlO_x$	SAPO-18	673	3	4500	2.0	40.2	44.6	8.4	74.1	86.6	5.1	–	[81]
$ZnAl_2O_4$	SAPO-18	673	3	4500	2.0	34.8	43.9	9.0	70.7	86.0	5.0	–	[82]
ZnO-$ZnAl_2O_4$	AlPO-18	673	6	3000	1.0	41.6	47.2	2.3	79.3	85.4	11.7	–	[83]
MOF-derived $ZnZrO_x$	SAPO-34	673	3	3600	2.0	22.5	45.5	3.2	79.7	92.6	4.2	–	[84]
$Zn_1Zr_4O_x$	SAPO-11	653	4.5	2400	1.0	30.4	49.0	2.0	–	23.0	69.8	–	[85]
$1CeZrO_x$-$2ZnZrO_x$	ZSM-5@Si	693	3.6	500	2.0	58.0	45.0	3.0	1.0	22.0	78.0	76.0	[86]
$Zn_xCe_{2-y}ZryO_z$	SAPO-34	573	0.1	5400	2.0	7.0	5.0	5.0	83.0	86.6	8.4	–	[87]
Zr-doped Zn/Al_2O_3	SAPO-34	673	1	3600	2.0	8.0	46.0	13.0	75.0	87.0	0.0	–	[88]
ZnCr alloy	beta	623	2.1	4978	2.0	33.0	49.0	7.0	–	71.0	22.0	–	[89]
ZnO	SAPO-34	663	4	1600	2.5	31.9	42.0	3.1	76.7	92.2	4.7	–	[90]
Cr-Zn	SAPO-34	673	1	3600	2.0	44.0	42.8	20.8	16.9	86.0	0.0	–	[91]
ZnCrAl alloy	ZSM-5	672	10	500	2.0	27.0	–	10.1	–	89.9	0.0	–	[92]
ZnO-Cr_2O_3	silicon-alumina	683	1.1	–	2.0	56.0	46.1	29.9	–	60.5	7.9	1.7	[93]

a) The T, P, GHSV, H_2/CO, X_{CO}, S_X (X = CH_4, $C^=_2$–$C^=_4$ alkene, C_2–C_4 alkane, C_{5+} and aromatics) represent the reaction temperature, total pressure, gas hourly space velocity, the feed gas ratio of H_2/CO, conversion rate of CO and selectivities of different products, respectively.

reaction was only 7.2% [42]. However, after a decade of intensive research, the CO conversion rate has now reached 85%, with the olefin selectivity exceeding 80% [43]. By changing the zeolite type, the products can be adjusted from methanol [26,44,45] to light olefin with CHA (SAPO-34 [8,46–51], SSZ-13 [52]), AEI (AlPO-18 [53], SAPO-18 [54], GeAPO-18 [43]), ERI (SAPO-17 [55]), MWW (MCM-22 [56]), MOR-Py [57] and SAPO-18/34 intergrowth [58] zeolite, ester with MOR zeolite [59], C_{5+} hydrocarbon with MWW (MCM-22 [60,61], MCM-49 [62]) zeolite and aromatic hydrocarbon with ZSM-5 zeolite [63–70]. Several reports also focused on CO_2 hydrogenation using $ZnCrO_x$-ZEO catalysts. For example, a $ZnCr_2O_4$|ZSM-5 catalyst [71] achieves the highest aromatic yield to 20.0%, as a similar yield (18.0%) also accomplished by nano-sized $ZnCr_2O_4$|Sbx-H-ZSM-5 system [72] with higher CO_2 conversion (37.5%) but lower aromatic selectivity (48.1%). Zn^{2+} was introduced by Zhang et al. [73] into ZSM-5 to enhance the selectivity of aromatics, although the reason was still under cover. Bao and co-workers [74] also reported $ZnCrO_x$ co-operating with phosphorus-modified ZSM-5 zeolite to shield the external acidic sites, synthesizing *para*-xylene in the presence of toluene with high selectivity (85.3%). Recently, Guo et al. [75] utilized $ZnCrO_x$|H-ZSM-5 to reduce CO_2 to trimethylbenzene (57.4% in aromatics) and ethylene (83.9% in light olefins) with high selectivity. Additionally, catalysts containing $ZnCrO_x$ and zeolite with TON (ZSM-22 [76]) and RTH (H-RUB-13 [77]) topology were also found to be selective for light olefin conversion, with 93% ethylene in light olefin and 74% light olefin species in total for ZSM-22, and 84% light olefin selectivity for H-RUB-13.

The conversion of CO_x on $ZnAl_2O_4$ had been shown to be more selective to methanol and resistant to sintering at high temperatures [94,95]. Its ability to convert CO_x to olefins via OX-ZEO catalyst is also attractive. Li and co-workers [78] first reported a hybrid Zn-Al_2O_3|SAPO-34 bifunctional catalyst for STO with a low CO conversion (4.5%) but high C_{2-4} olefin selectivity (77%). Subsequently, a $ZnAlO_x$|SAPO-34 achieving a higher CO conversion (6.9%) has been reported with C_{2-4} olefins selectivity reaching 77.0% in hydrocarbons and only 33.1% CO_2 selectivity under reaction conditions of H_2:CO = 1:1, space velocity = 12000 mL g^{-1} h^{-1}, 4.0 MPa and 663 K [19]. Wu and co-workers [79] utilized $ZnAlO_x$ with boron-assisted CHA type zeolite to achieve the highest light olefin selectivity (85.1%) with moderate CO conversion (10%). Wang and co-workers [18,80] developed a $ZnAl_2O_4$|SAPO-34 catalyst with enhanced 24% CO conversion and 80% C_{2-4} olefins selectivity. They also tested a series of zeolites cooperating with $ZnAl_2O_4$, including SAPO-11, SAPO-17, SAPO-18, SAPO-31, SAPO-35. Among these, SAPO-17 showed 23% CO conversion and 65.8% light olefin selectivity, while SAPO-11 and SAPO-31 exhibited high C_{5+} species selectivity [80]. The highest CO conversion rate for STO was achieved on $ZnAlO_x$|AEI topology zeolite (SAPO-18 [81,82], AlPO-18 [83]) catalysts, with CO conversion >40% and 75%–80% C_{2-4} olefin selectivity. The $ZnAl_2O_4$ also achieved methyl acetate (MA) and acetic acid (AA) selectivity of 85% and CO conversion of 11% at 643 K with a $ZnAl_2O_4$|H-MOR bifunctional catalyst [59]. Moreover, the $ZnAlO_x$ catalyst demonstrated excellent catalytic

Table 2 Zn-based OX-ZEO bifunctional catalysts reported for CO_2 hydrogenation to various hydrocarbons and their performance

Oxide	Zeolite	T (K)	P (MPa)	GHSV	H_2/CO	X_{CO_2}	S_{CO}	S_{CH_4}	$S_{C_2^=-C_4^=}$	$S_{C_2-C_4}$	$S_{C_{5+}}$	$S_{Arom.}$	Ref.
$ZnZrO_x$	Zn-modified SAPO-34	653	2	3600	3.0	12.6	47.0	3.0	80.0	94.0	3.0	–	[10]
$ZnAlO_x$	ZSM-5	593	3	6000	3.0	6.0	55.0	0.4	19.3	19.3	80.3	73.9	[11]
$ZnAl_2O_4$	SAPO-34	643	3	5400	3.0	15.0	49.0	1.0	87.0	10.0	2.0	–	[18]
$ZnCr_2O_4$	ZSM-5	623	4	1200	3.9	23.4	27.3	0.5	3.0	9.3	87.1	85.3	[71]
$ZnCr_2O_4$	Sbx-H-ZSM-5	623	2	300	3.0	37.5	85.0	1.7	–	38.3	60.0	48.1	[72]
$ZnCrO_x$	ZnZSM-5	593	5	2000	3.0	19.9	72.0	1.5	10.0	28.8	69.5	56.5	[73]
$ZnCrO_x$	ZSM-5	663	4	15000	3.0	15.0	70.4	0.7	9.1	10.3	89.0	87.7	[74]
$ZnCrO_x$	H-ZSM-5	603	3	3000	3.0	17.5	40.0	3.0	26.1	35.1	69.6	64.6	[75]
$ZnCr_2O_4$	ZSM-22	633	5	1200	3.1	21.9	57.6	7.5	25.6	74.0	13.3	–	[76]
$ZnZrO_x$	H-RUB-13	623	3	4000	3.0	16.0	28.0	2.0	75.0	85.0	13.0	–	[77]
$ZnCrO_x$	H-RUB-13	623	3	4000	3.0	14.0	54.0	1.0	84.0	90.0	9.0	–	[77]
$Mg\text{-}ZnZrO_x$	H-RUB-13	623	3	4000	3.0	11.0	32.0	5.0	64.0	89.0	10.0	–	[77]
$ZnAl_2O_4$	SAPO-34	593	3	1500	3.0	14.0	54.0	1.0	87.0	98.0	0.8	–	[96]
$ZnAl_2O_4$	SAPO-18	593	3	1500	3.0	15.0	63.0	1.8	84.0	93.8	4.2	–	[96]
$ZnAl_2O_4$	H-SSZ-13	643	3	5400	3.0	14.0	60.0	2.0	1.6	95.0	1.4	–	[96]
$ZnAl_2O_4$	H-ZSM-11	643	3	5400	3.0	14.0	58.0	0.6	1.4	34.0	64.0	57.0	[96]
$ZnAl_2O_4$	H-ZSM-5	643	3	5400	3.0	11.0	60.0	1.9	8.0	10.0	80.0	72.0	[96]
$ZnAl_2O_4$	H-MOR	643	3	5400	3.0	17.0	60.0	3.0	9.1	85.0	2.9	–	[96]
$ZnAl_2O_4$	H-Beta	643	3	5400	3.0	16.0	60.0	2.5	3.5	74.0	20.0	1.0	[96]
$ZnZrO_x$	MOR	648	1	2100	3.0	20.9	72.9	8.8	49.0	91.2	0.0	–	[97]
$ZnZrO_x$	FER	648	1	2100	3.0	23.5	90.1	0.0	26.3	61.6	38.4	–	[97]
$ZnZrO_x$	MFI	648	1	2100	3.0	22.0	57.6	2.9	29.5	66.2	30.9	–	[97]
$ZnZrO_x$	SAPO-34	648	1	2100	3.0	17.9	72.7	6.5	45.4	93.5	0.0	–	[97]
$ZnZrO_x$	SSZ-13	648	1	2100	3.0	28.0	70.8	4.9	16.8	85.3	10.0	–	[97]
$ZnZrO_x$	ERI	648	1	2100	3.0	23.6	80.7	7.7	38.8	92.3	0.0	–	[97]
$ZnZrO_x$	SAPO-34@UIO-66	653	3	6000	3.0	14.0	50.0	3.0	78.0	96.0	1.0	–	[98]
$ZnZrO_x$	Bio-SAPO-34	653	3	8000	3.0	13.8	40.0	1.0	83.0	99.0	0.0	–	[99]
$Mg\text{-}ZnZrO_x$	SAPO-34	663	2	12000	3.0	17.0	53.0	8.0	83.0	90.0	3.0	–	[100]
$ZnZrO_2@Al_2O_3$	SAPO-34	653	3	3500	3.0	21.0	45.0	3.0	75.0	95.0	2.0	–	[101]
$ZnZrO_x$	SAPO-34	653	3	6000	3.0	40.0	53.5	2.4	74.2	91.6	6.0	–	[102]
$ZnZrO_x$	SSZ-13	633	2	4500	3.0	9.1	32.0	2.0	89.4	95.9	2.0	–	[103]
$ZnZrO_x$	ZSM-5	593	4	1800	3.0	14.0	44.0	0.0	4.0	18.0	82.0	78.0	[104]
$ZnZrO_x$	$ZSM\text{-}5@SiO_2$	613	3	15000	3.0	12.0	80.0	2.0	4.0	21.0	77.0	75.0	[105]
$ZnZrO_x$	H-ZSM-5	588	3	1020	3.0	17.0	23.0	3.0	15.0	28.0	69.0	60.0	[106]
$ZnZrO_x$	H-ZSM-5	598	3	4800	3.0	15.2	41.3	5.7	–	32.6	22.0	63.9	[107]
$ZnZrO_x$	$H\text{-}ZSM\text{-}5\text{-}1.5NH_4F$	598	3	4800	3.0	17.6	36.3	5.5	–	16.9	78.5	77.5	[108]
$ZnZrO_x$	Mg-Si-ZSM-5	593	2	4800	3.0	7.0	22.0	0.0	–	53.0	47.0	20.0	[109]
$ZnZrO_x$	MFI	648	1	2118	3.0	26.0	54.0	4.3	26.1	50.0	43.5	–	[110]
$ZnZrO_x$	H-MFI	623	3	4800	3.0	20.5	33.5	0.7	30.9	47.5	51.8	–	[111]
$ZnZrO_x$	H-MOR	623	3	4800	3.0	15.9	41.2	5.6	47.5	83.4	11.0	–	[111]
$ZnZrO_x$	ZSM-11	573	3	1200	3.0	8.0	52.0	0.0	6.0	18.0	82.0	78.0	[112]
$ZnO\text{-}ZrO_2$	ZSM-5	613	4	7200	3.0	15.0	38.0	0.3	6.6	12.8	80.3	76.0	[113]
$ZnO\text{-}ZrO_2$	ZSM-5	613	3	4800	3.0	9.1	42.5	0.6	8.1	14.6	85.9	70.0	[114]
$ZnZrO_x$	Bio-ZSM-5	663	3	2000	3.0	10.5	82.0	5.5	64.4	94.5	0.0	–	[115]
$In\text{-}ZnZrO_x$	nano-ZSM-5	598	3	4000	3.0	13.8	19.8	0.2	1.5	7.0	92.0	90.0	[116]
$ZnZrO_x$	$ZSM\text{-}5@n\text{-}ZrO_2$	613	2	15600	3.0	9.5	34.3	1.0	81.1	98.0	1.0	–	[117]

performance for CO_2 hydrogenation. The $ZnAlO_x$|H-ZSM-5 catalyst achieved 73.9% aromatics selectivity with 9.1% CO_2 conversion with H_2:CO_2 = 3:1, 3.0 MPa, 593 K [11]. The $ZnAlO_x$|SAPO-34 also effectively reduced CO_2 to produce light olefins, resulting in 87% C_{2-4} olefins selectivity and 15% CO_2 conversion [18]. Guo et al. [77] reported a $ZnAlO_x$|H-RUB-13 catalyst that suppressed the reverse water-gas shift (RWGS) to only 32% CO selectivity, with 11% CO_2 conversion and 64% light olefin selectivity. Wang and co-workers [96] investigated the catalytic performance of spinel $ZnAl_2O_4$ and several zeolites (SAPO-34, SAPO-18, H-SSZ-13, H-ZSM-11, H-ZSM-5, H-MOR and H-Beta). They found the highest light olefin selectivity (87%) with SAPO-34, the highest propane selectivity (80%) with H-SSZ-13 and the highest aromatic selectivity (72%) with H-ZSM-5.

The $ZnZrO_x$ catalyst holds significant promise in CO_x hydrogenation due to its non-toxicity, long-term durability, and excellent catalytic performance in converting CO_x to methanol, olefins, and aromatics. Wang and co-workers [41] first reported the $ZnZrO_x$|SAPO-34 bifunctional catalyst for efficient STO conversion, offering 9.2% CO conversion and 74% C_{2-4} olefin selectivity. They further optimized the CO conversion by controlling the Zn/Zr ratio to adjust the hydrogenation ability of the oxide, achieving 28% CO conversion and 76% C_{2-4} olefin selectivity with Zn-doped ZrO_2|SSZ-13 catalyst [20]. Alternatively, Zhang et al. [84] synthesized MOF-derived $ZnZrO_x$|SAPO-34 bifunctional catalyst via a Zn-UiO-66 calcination method, promoting CO conversion to 22.5%. Liu et al. [85] reported a $Zn_1Zr_4O_x$|SAPO-11 catalyst with 30.4% CO conversion and 69.8% C_{5+} selectivity. The highest olefin/aromatics conversion rate was achieved by incorporating $CeZrO_x$ into $ZnZrO_x$ to decouple the active sites for CO adsorption and H_2 activation, elevating CO conversion to 58% with 76% aromatics selectivity on 1$CeZrO_x$-2$ZnZrO_x$|ZSM-5@Si catalyst [86]. Significant researches have focused on CO_2 hydrogenation with $ZnZrO_x$ catalysts, compared to CO hydrogenation. Li and co-workers [10] first reported $ZnZrO_x$|Zn-modified SAPO-34 for CO_2 hydrogenation, achieving 12.6% CO_2 conversion and 80% light olefin selectivity, resulting in 10% CO_2 conversion rate. Similar conversion rates (ranging from 8% to 12%) were achieved with various modification to SAPO-34 zeolite in $ZnZrO_x$|SAPO-34 catalysts [97–99]. Strengthening CO_2 adsorption by introducing MgO into $ZnZrO_x$ increased CO_2 conversion, achieving conversion rates up to 14% [100]. The stability of active sites during the hydrothermal treatment was advanced by post pre-coating $ZnZrO_2$ with Al_2O_3, resulting in a 16% CO_2 conversion rate with $ZnZrO_2$@Al_2O_3@SAPO-34 catalyst [101]. Wang et al. [102] further elevated the CO_2 conversion rate to approximately 30% using 12–18 nm $ZnZrO_x$ nanoparticles with SAPO-34. Zeolite with similar topology was also reported by Kenta and co-workers [97], utilizing $ZnZrO_x$|SSZ-13 with 28% CO_2 conversion but poor C_{2-4} olefin selectivity (16.8%). Li and co-workers [103] optimized the catalyst with $ZnZrO_x$ dispersing on SSZ-13, achieving an 8% CO_2 conversion rate with 89.4% C_{2-4} olefin selectivity. Guo et al. [77] found that a $ZnZrO_x$|H-RUB-13 catalyst suppressed the RWGS reaction with no obvious decrease in CO_2 conversion rate (12%). There are also notable results for converting CO_2 to aromatics. Li et al. [104] reported a $ZnZrO_x$|ZSM-5 catalyst with 14% CO_2 conversion and 78% aromatics selectivity, thus the total aromatics production rate reaching 11%. Changing the distance between $ZnZrO_x$ and the zeolite [105], or altering zeolite surface structures using nanocrystals [106], introducing Zn^{2+} ion [107] or using NH_4F [108] did not effectively affect the CO_2 conversion rate, which remained within the range of 9%–14%. The introduction of MgO and SiO_2, as reported by Li and co-workers [109], significantly enhanced the selectivity of *para*-xylene from CO_2 hydrogenation, though the CO_2 conversion rate severely suffered (<1.5%). Iyoki and co-workers [97,110,111] utilized the $ZnZrO_x$|H-ZSM-5 to produce light hydrocarbons, achieving CO_2 conversion within 20%–26% and light hydrocarbon selectivity ranging from 47%–66%, depending on the pre-treatment of H-ZSM-5. They also reported moderate catalytic performance when $ZnZrO_x$ was combined with other topological zeolites (MOR [97,111], FER [97] and ERI [97]). Additionally, Li and co-workers [112] developed a unique $ZnZrO_x$|ZSM-11 catalyst with 8% CO_2 conversion and 78% aromatic selectivity.

Although the catalyst systems vary largely, the C_{2+} product yield for CO_x hydrogenation is still less than 50%, offering an ample room for further improvement (Figure 1). The design of new catalysts would rely heavily on the deep understandings of the catalytic active sites and reaction mechanisms. As general aspects of syngas or CO_2 conversion have been reviewed over the past few decades [118–122], here we aim to provide a comprehensive review on the catalytic active sites and reaction mechanism of CO_x hydrogenation on Zn-based catalysts from a fundamental point of view. The following sections will serve to discuss the catalytic active sites on three typical Zn-based mixed oxide catalysts (Section 2) and explore the reaction mechanisms of CO_x hydrogenation on these Zn-based mixed oxide catalysts (Section 3). The challenges and the future research directions are outlooked at the end.

2 Catalytic active sites on Zn-based mixed oxide catalyst

2.1 $ZnCrO_x$

Numerous research groups have demonstrated that the Zn:Cr ratio plays a crucial role in influencing the catalytic activity and selectivity of both syngas-to-methanol and STO processes [26,123–125]. Despite the general belief that stoi-

chiometric $ZnCr_2O_4$ in a spinel crystal form is the most stable phase formed after calcination at high temperatures, it has been observed that $ZnCrO_x$ catalysts with a Zn:Cr ratio of 1:2 exhibit poor catalytic performance. For instance, the syngas-to-methanol activity is below 5 g kg cat^{-1} h^{-1} with only 14% selectivity to methanol [123], and CO conversion is below 30% for the STO reaction [126]. Conversely, increasing the Zn:Cr ratio to 1:1 significantly enhances CO conversion, leading to higher product selectivity. The optimal catalytic activity and selectivity for syngas-to-methanol are typically achieved with a Zn:Cr ratio of 1:1, resulting in a methanol yield of around 90 g kg cat^{-1} h^{-1} and a selectivity of 80% [123]. Similarly, for STO, CO conversion increases to 70%, with olefin selectivity exceeding 80% with Zn:Cr ratio in the range of 1:0.59 [126]. Therefore, understanding the structure of $ZnCrO_x$ with a Zn:Cr ratio greater than 1:1 is of utmost importance, particularly as the real surface structure of $ZnCrO_x$ under reaction conditions remains a subject of debate.

According to one perspective, the structure of $ZnCrO_x$ with a Zn:Cr ratio larger than 1:1 comprises a combination of spinel $ZnCr_2O_4$ and a ZnO layer. Various models have been proposed to represent the active sites within this structure, including $ZnCr_2O_4$ surfaces, Cr-doped ZnO, Zn-doped Cr_2O_3, and the $ZnCr_2O_4$//ZnO interface. Specifically, for the $ZnCr_2O_4$ spinel surfaces, our previous work [127] demonstrated that the most stable $ZnCr_2O_4$ (111) surface exhibits inert behavior toward syngas conversion, aligning with experimental results [41,123]. However, highly reduced $ZnCr_2O_4$ surfaces may exhibit good catalytic performance. Xiao and co-workers [128] investigated the reaction network of syngas conversion on the reduced $ZnCr_2O_4$ (111) surface (Figure 2a) with a high concentration of O_Vs. Their study revealed that the presence of 50% to 75% O_V concentration significantly reduces the reaction energy barrier for syngas-to-methanol conversion. Notably, they observed that CH_2CO exhibits a higher total reaction rate compared to CH_3OH under STO condition, with turnover frequencies (TOFs) of 71.6 and 1.94, respectively. Hu and co-workers [129] have investigated the STO reaction pathways on the reduced $ZnCr_2O_4$ (110) surface (Figure 2b). They observed that the surface featuring two adjacent two-coordinate O_Vs (denoted as V_{O2C}) is favored for the initial adsorption of CO. Subsequently, hydrogen-assisted C–O bond breaking occurs, leading to the formation of intermediate CHO adsorbents, which significantly influence product selectivity. They claimed that if the surface is only mildly reduced with diluted V_{O2C} existing, CO could undergo continuous hydrogenation, giving CH_3OH an advantage over CH_2CO. However, whether these high-concentration O_Vs exist under reaction conditions is still an open question.

For the doped model, Li and co-workers [130] investigated the activation of CO and H_2 on Cr-doped ZnO and Zn-doped

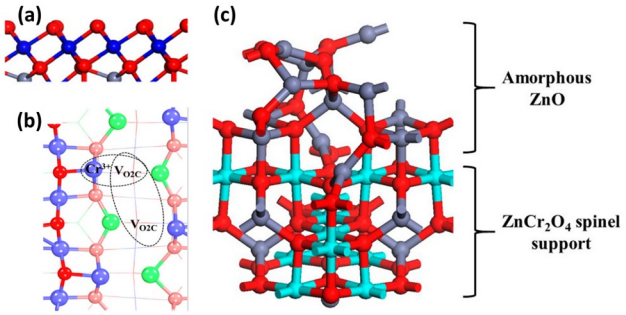

Figure 2 (Color online) Various active surface structures hypothesized on zinc-chromium oxide catalyst in syngas conversion process. (a) O-terminated $ZnCr_2O_4$ (111) surface with Cr at subsurface. Copyright with permission of American Chemistry Society of ref. [128]. (b) $ZnCr_2O_4$ (110) surface with adjacent two oxygen vacancies (denoted as V_{O2C}). Copyright with permission of American Chemistry Society of ref. [129]. (c) $ZnCr_2O_4$// ZnO double layered structure model. Copyright with permission of John Wiley and Sons of ref. [69].

Cr_2O_3 surface models, resulting from ZnO/Cr_2O_3 mixed phase. The Cr_1-substituted ZnO $(10\bar{1}0)$ surface has been synthesized and reported stable under diverse temperature and pressure conditions [131]. The pristine ZnO $(10\bar{1}0)$ surface is active for H_2 heterolytic dissociation, and the presence of Cr_1 increases the formation energy of O_Vs, lowering the reactivity of H_2 dissociation. Conversely, the pristine Cr_2O_3 (001) surface exhibits a lower formation energy of O_Vs, promoting reactivity even higher than that of ZnO $(10\bar{1}0)$ after the introduction of Zn_1 atom. Enhanced H_2 activation has been reported on Zn_1-substituted Cr_2O_3 surface while no improvement was found on Cr_1-substituted ZnO. The doped model provides new insights into designing heterometal oxide catalysts, although no reaction pathways on syngas conversion were developed.

For the $ZnCr_2O_4$//ZnO interface model (Figure 2c), Tan and co-workers [69] reported the synergistic effect of $ZnCr_2O_4$ and ZnO on the $ZnCrO_x$ spinel surface by physically mixing two components to avoid the formation of ambiguous non-stoichiometric structures. Electron paramagnetic resonance (EPR) spectra of various ZnO ratios show that the O_Vs increase with the addition of ZnO, and more oxygenates generated from syngas are observed with *in-situ* Fourier transform-infrared spectroscopy (FT-IR), indicating that the synergistic effect influences the adsorption and conversion of intermediates. Bao and co-workers [126] found that the CO conversion strongly depends on the Cr:Zn ratio for the STO reaction on $ZnCrO_x$-SAPO-18 catalyst with the maximum CO conversion reached at a Cr:Zn ratio of 0.44:1 (Figure 3a). High-resolution scanning transmission electron microscopy-electron energy loss spectroscopy (HRSTEM-EELS) revealed a clear dependence of the C–O dissociation activity on the surface structure (Figure 3b–e). The narrow $ZnCr_2O_4$ (110) facets (≤1 nm width), constrained between the (311) and (111) facets, had an enriched ZnO_x

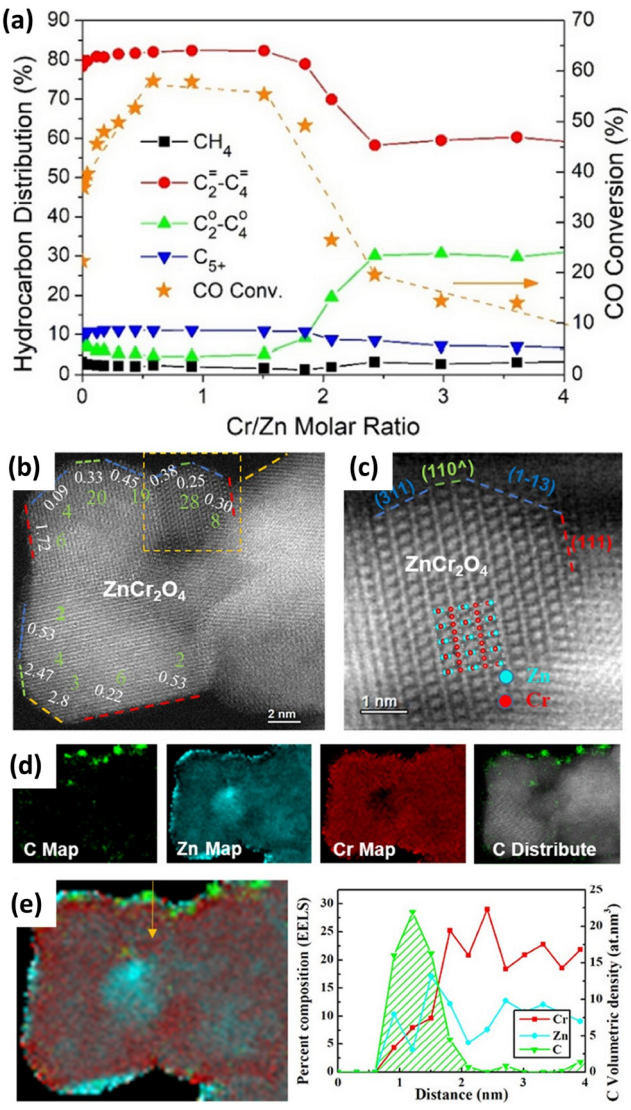

Figure 3 (Color online) (a) CO conversion and product distribution as a function of the Cr/Zn(n) molar ratio over $ZnCr_n$-SAPO-18 composite catalysts. Reaction conditions: 400 °C, 4.0 MPa, GHSV = 3000 mL g_{cat}^{-1} h^{-1}, H_2/CO = 2.5, and OX/ZEO = 2. (b–e) STEM-EELS mapping of surface carbon species, and elemental distribution of Cr and Zn over $ZnCr_{0.44}$ upon catalyzing CO dissociation. (b) ADF image of $ZnCr_2O_4$ spinel survey area, viewed from the [112] axis, with the green dashed line standing for the narrow surface junctions along the $ZnCr_2O_4$(110) facet constrained between the (311) and (111) facets; the white number showing the surface Cr/Zn ratio and the green number showing the volumetric density of carbon species on the corresponding surface. (c) HRSTEM image of the highlighted region of figure (b), with the inset illustrating the atomic structure of $ZnCr_2O_4$ spinel. (d) C, Cr, and Zn maps. (e) Line profile along the arrow across the ZnO_x©$ZnCr_2O_4$(110) surface. Copyright with permission of American Chemistry Society of ref. [126].

overlayer. The line scanning analysis demonstrated that these surfaces are characterized by an atomic overlayer of ZnO_x but a deficiency of zinc in the subsurface (at a depth of 2 nm). Their surface carbon density was two to three times higher than that over the surface of $ZnCr_2O_4$(311) and $ZnCr_2O_4$(111) with an atomic ZnO_x overlayer. It was an order of magnitude higher than that over thick ZnO_x layers, pure ZnO, and the stoichiometric $ZnCr_2O_4$ surfaces of various facets. Song et al. [123] proposed a model with double-layer amorphous ZnO supported on spinel $ZnCr_2O_4$ bulk, possessing the lowest O_V formation energy among various surface structure candidates. As a result, the lowered O_V formation energy should promise higher activity for both STO and syngas-to-methanol.

Another opinion proposed a non-stochiometric $ZnCrO_x$ spinel phase is the catalytic active phase [44,45,124,127,132]. Tian et al. [132] revealed that zinc-rich $ZnCrO_x$ with the best catalytic performance does not show the presence of ZnO, as proved by high resolution transmission electron microscope (HRTEM) and X-ray diffraction (XRD). The X-ray adsorption near edge structure (XANES) and extended X-ray absorption fine structure (EXAFS) analyses further indicated that the local environment of Zn and Cr differs significantly from those in ZnO foil and Cr_2O_3. Tian et al. [133] also applied the XANES and EXAFS to fresh and used $ZnCrO_x$ catalysts. They identified two striking features associated with catalyst deactivation at ~9668 and ~9680 eV, respectively, implying that some Zn ions transition from $[ZnO_4]$ to $[ZnO_6]$ environment [133].

Recently, we proposed a non-stochiometric $Zn_3Cr_3O_8$ spinel phase (Figure 4a) utilizing a global neural network (NN) and stochastic surface walking (SSW) global potential energy surface (PES) sampling method [127]. We constructed the Zn-Cr-O ternary phase diagram within the range of Zn:Cr = 0:1 to 1:1. The $ZnCr_2O_4$ crystal from early experimental reports falls in the spinel region depicted in green, and the thermodynamically stable spinel bulks from PES global minimum are limited to the red dashed region. Among these, a newly identified $Zn_3Cr_3O_8$ exhibits the highest concentration (12.5%) of the unusual $[ZnO_6]_{Oh}$ in the bulk, correlating with higher catalytic activity. Under a syngas atmosphere, the spinel $Zn_3Cr_3O_8$ surface can undergo reduction with the higher O_V concentration than $ZnCr_2O_4$. Particularly, the formation of subsurface O_V leads to an unprecedented planar $[CrO_4]_{pla}$ site, instead of previous reported pyramid $[CrO_5]_{pyr}$ (Figure 4b), that forms dynamically under reaction conditions, reducing the reaction barrier of syngas-to-methanol process to approximately 1.2 eV. The density of states (DOS) of $ZnCr_2O_4$ (111) and $Zn_3Cr_3O_8$ (0001) surface under syngas atmosphere reveals the intrinsic difference between two typical surfaces, as depicted in Figure 4c, d. The excess electrons after reduction on $ZnCr_2O_4$ (111) surface locates above the bulk oxide valance band maximum, owing to Cr^{3+} in the $[CrO_5]_{pyr}$ geometry. However, on $Zn_3Cr_3O_8$ (0001) surface, the excess electrons are stabilized within the conductive band due to the Cr^{2+} in $[CrO_4]_{pla}$ geometry. The high energy electrons on $ZnCr_2O_4$ (111) surface flows towards surface oxo species (CH_nO), leading to a strong adsorption and thus hinders the syngas-to-methanol process.

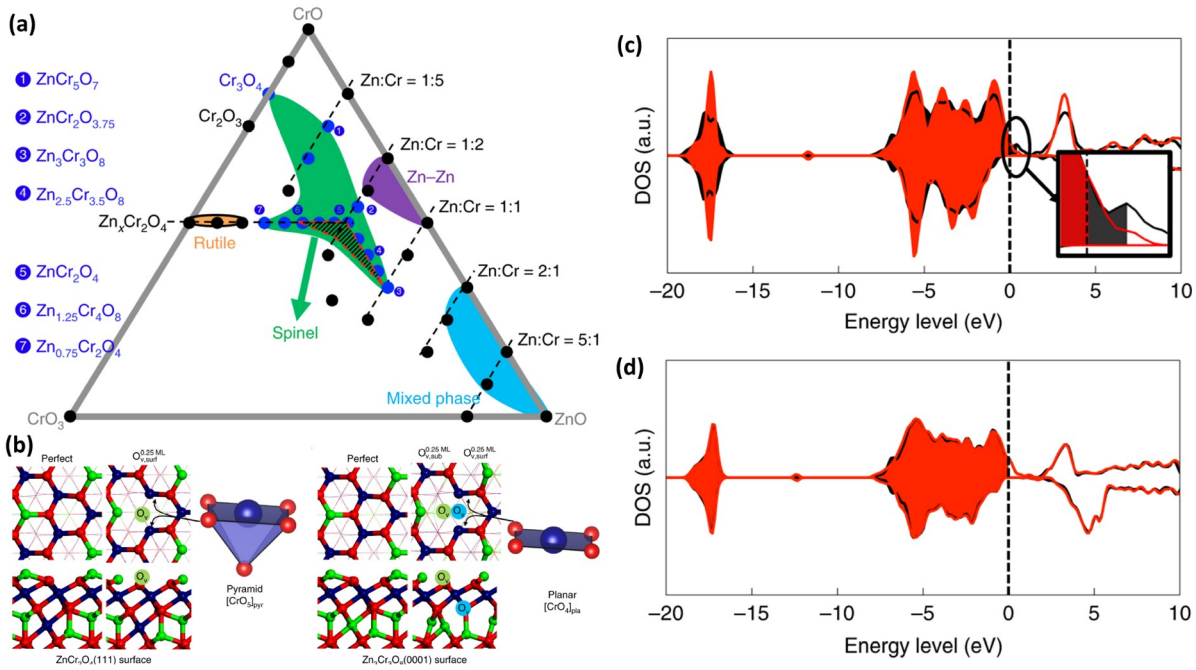

Figure 4 (Color online) (a) Ternary Zn-Cr-O phase diagram. The green region maps out that the compositions with the spinel-type skeleton structure as the global minimum; the blue circles labelled by numbers indicate the composition. Only the spinel ZnCrO phases in the red dashed triangle are thermodynamically allowed. (b) The perfect O_V containing $ZnCr_2O_4$ $O_{V,surf}^{0.25\ ML}$ (111) and $Zn_3Cr_3O_8$ $O_{V,surf}^{0.25\ ML}$ $O_{V,sub}^{0.25\ ML}$ (0001) surface structures. The $[CrO_5]_{pyr}$ and $[CrO_4]_{pla}$ configurations near to an O_V are highlighted. The surface/subsurface O_V concentration of 0.25 ML with respect to all the O atoms in the same layer is denoted as $O_{V,surf}^{0.25\ ML}/O_{V,sub}^{0.25\ ML}$. (c, d) DOS before (black) and after (red) CH_3O adsorption on the (c) $ZnCr_2O_4$ $O_{V,surf}^{0.25\ ML}$ (111) and (d) $Zn_3Cr_3O_8$ $O_{V,surf}^{0.25\ ML}$ $O_{V,sub}^{0.25\ ML}$ (0001) surfaces. Copyright with permission of Nature of ref. [127].

We further simulated the XANES spectra of $ZnCr_2O_4$ and $Zn_3Cr_3O_8$, and found that the first peak at ~9668 eV shifts to a higher energy level as Zn:Cr ratio increases. These results are well consistent with the experimental results, in which fresh and used catalysts show similar XANES variation trends after catalyst deactivation [133]. This suggested that the real $ZnCrO_x$ surface in the STO process was likely the non-stoichiometric spinel with a high Zn:Cr ratio, while the ZnO-$ZnCr_2O_4$ surface forms during deactivation process.

In summary, although various $ZnCrO_x$ catalyst models have been proposed to elucidate active sites, they consistently highlight the formation of high concentrations of O_V. This common finding underscores the significance of O_V in these catalysts. Specifically, the high concentration of O_V leads to a reduction in the coordination numbers of Zn and Cr atoms. This reduction enhances the catalyst's capability to adsorb hydrogen (H_2) and carbon monoxide (CO), thereby impacting its catalytic activity.

2.2 $ZnAlO_x$

The $ZnAlO_x$ catalyst, specifically the $ZnAl_2O_4$, is a typical normal spinel structured oxide with a wide energy band gap (3.8–3.9 eV). As a result, it has been widely used in semiconductors, sensors and heterogeneous catalysis due to its low surface acidity, high thermal stability and superior hydrophobicity [134]. $ZnAl_2O_4$|ZEO bifunctional catalysts have been reported for both CO and CO_2 hydrogenation process, as shown in Figure 1. It should be noted that the catalytic performance of $ZnAlO_x$, whether for the conversion of CO or CO2 species, is still limited compared to state-of-the-art catalysts using other oxides, $ZnCrO_x$ and $ZnZrO_x$. The total conversion rate is under 35% for CO hydrogenation and under 20% for CO_2 hydrogenation. However, the performance of $ZnAlO_x$ catalysts falls within the range of most published results for $ZnCrO_x$ and $ZnZrO_x$, implying that there might be potential for improvement. Unfortunately, only few studies have focused on $ZnAl_2O_4$ due to its low catalytic activity and the complex surface characteristics of spinel oxides, which make it challenging to identify surface structures, understand reaction mechanism, and thus make further improvements on catalyst performance [94,135,136].

The important surface species and critical surface structures involved in the syngas-to-methanol process over the spinel $ZnAl_2O_4$ catalyst has been thoroughly investigated using *in situ* high temperature/pressure magic angle spinning (MAS) nuclear magnetic resonance (NMR) technology. The results reveal that CO tends to insert into Al_{IV} hydroxyl sites, forming the key intermediate, formate species. This intermediate then prefers to occupy the Zn_{III}-O_V site in close proximity with active Al_{IV}-OH groups. Consequently, the bidentate formate species was identified to coordinate on

-Al_{IV}-OH…Zn_{III}- dual active sites [137]. Yang and co-workers [136] investigated the reaction network of syngas-to-methanol on various $ZnAl_2O_4$ surfaces, namely $ZnAl_2O_4$ (100), $ZnAl_2O_4$ (110) and $ZnAl_2O_4$ (111) via a combination of periodic density functional theory (DFT) calculation and microkinetic simulation. They found that the O-terminated and hydroxylated surfaces were the possible active surfaces under reaction condition, with the stability of these surface decreasing in the order of (110)-B-1/4H > (111)-B-3/8H > (110)-B-1/4H, as shown in Figure 5a. Among these, the (111)-B-3/8H possesses unique electron holes near Fermi energy levels and thus is identified as the most active surface in the syngas-to-methanol process; while the other two have little low-energy valence bands and exhibit overall barriers greater than 1.9 eV with TOFs less than 10^{-2} s^{-1} at 673 K and 4 MPa H_2 pressure.

However, experimental evidence suggests that compared to the stoichiometric $ZnAl_2O_4$ spinel structure, the non-stoichiometric $ZnAlO_x$ catalyst with a Zn:Al ratio greater than 1:2 exhibits higher CO_x conversion rates. For example, a Zn-Al binary oxide catalyst with Zn/Al = 2:1 ratio, instead of previously reported spinel $ZnAl_2O_4$, has the highest methanol formation rate. The X-ray photoelectron spectroscopy (XPS) spectra in Figure 5b, monitoring fresh and spent Zn_2AlO_x, indicated that the content of $ZnAl_2O_4$ decreased from 46% (fresh Zn_2AlO_x) to 27% (spent Zn_2AlO_x), while that the content of ZnO increased from 54% (fresh Zn_2AlO_x) to 73% (spent Zn_2AlO_x). This suggests the critical role of amorphous ZnO and the interfaces of ZnO-Al_2O_3 and/or ZnO-$ZnAl_2O_4$. The high activity was believed to stem from the easier formation of O_V in ZnO due to the absence of strong Al-O bonds [138].

Similarly, a high CO conversion of 41.6% with a C_{2-4} olefin selectivity of 79.3% is achieved with a Zn/Al ratio of 1:1 by Xie and co-workers [83]. The scanning transmission electron microscopy (STEM) image in Figure 5c, d clearly shows that only several lattice stripes of spinel $ZnAl_2O_4$ are displayed in $ZnAlO_x$ sample with Zn:Al = 1:2, while that of both spinel $ZnAl_2O_4$ and ZnO are shown in sample with Zn:Al = 1:1. The XANES and EXAFS spectra of Zn_1AlO_x demonstrate the existence of Zn-Al and Zn-Zn in the second coordination shell, closely resembling that of $ZnAl_2O_4$ and ZnO. They believed that the $ZnAl_2O_4$ spinel is the main active site for CO activation, while its strong Lewis acid sites severely adsorb methanol, inhibiting methanol desorption and acting like a "trap" in the catalytic pathways. The presence of ZnO nanoparticles greatly suppresses the exposure of strong acidic sites, according to NH_3-TPD result, serving as an anti-trap effect to improve the desorption of methanol.

Zhang et. al. [138] proposed a reaction-driven reconstructed amorphous ZnO-$ZnAl_2O_4$ double-layered model based on *in situ* experimental evidences. During the syngas-to-methanol conversion process, a 12-h induction period exists for the spinel $ZnAl_2O_4$ catalyst, implying possible

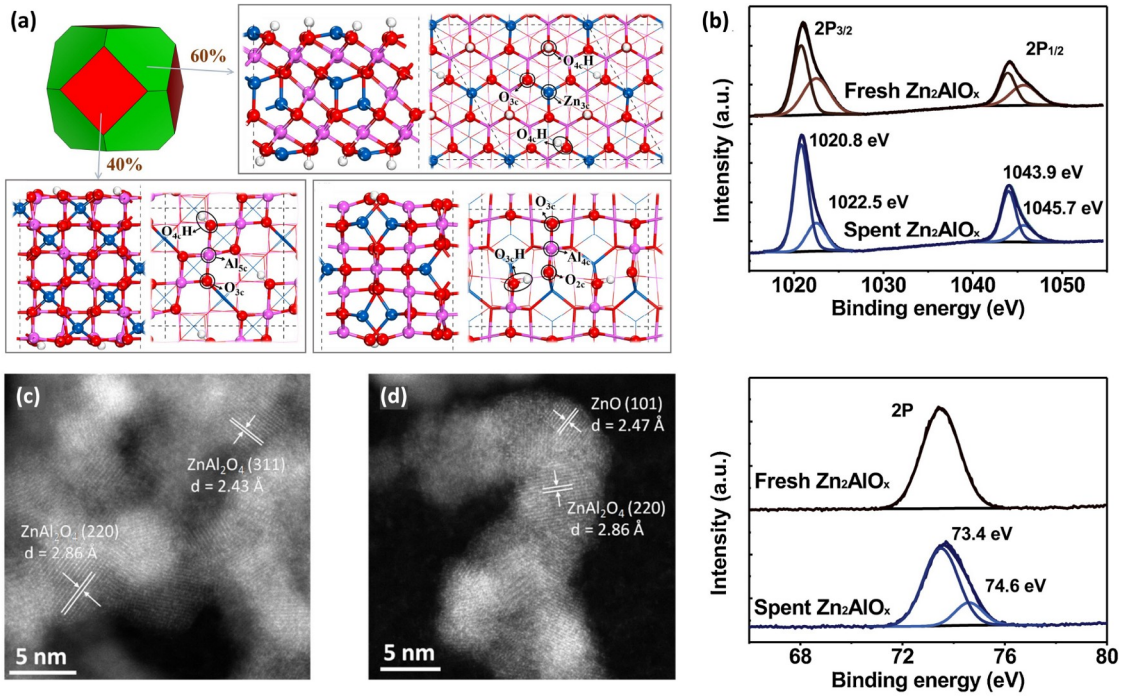

Figure 5 (Color online) (a) Simulated structure of $ZnAl_2O_4$ particle at 298 K according to the Wulff construction rule, containing the most stable structures of $ZnAl_2O_4$(111), $ZnAl_2O_4$(100) and $ZnAl_2O_4$ (110) surface. Copyright with permission of Elsevier from ref. [136]. (b) Zn 2p (upper) and Al 2p (bottom) XPS spectra of fresh Zn_2AlO_x and spent Zn_2AlO_x. Copyright with permission of Elsevier from ref. [138]. (c, d) Aberration-corrected STEM images of $Zn_{0.5}AlO_x$ (c) and Zn_1AlO_x (d). Copyright with permission of American Chemistry Society from ref. [85].

surface structural changes of the catalyst. However, XRD shows no difference between spent and fresh catalyst, indicating that the bulks structures remain identical. The absence of hydrogenated carbonate species peak on Al sites (Al-OCOOH) in the spent $ZnAl_2O_4$ catalyst, as observed by *in situ* FT-IR and Raman spectroscopy, along with the high-resolution STEM images, reveals that amorphous ZnO segregates on the surface of reconstructed $ZnAl_2O_4$ catalyst, promoting H_2 activation and facilitating faster methanol conversion.

In conclusion, the surface of $ZnAlO_x$ under reaction condition is believed to consist of spinel $ZnAl_2O_4$ and amorphous ZnO due to the presence of excess Zn atoms. $ZnAlO_x$ catalyst, similar to $ZnCrO_x$ system, with Zn:Al ratio > 1:2 has shown higher reaction activity and selectivity, although their surface structures might be varied. The synergic interaction between hydrogen on Zn-O-Zn surface and carbon species on adjacent Zn-O-Al interface has been identified as the most likely active sites, explaining the privileged performance of zinc-rich $ZnAlO_x$.

2.3 $ZnZrO_x$

Unlike other Zn-based oxide catalysts with high Zn content, such as $ZnCrO_x$ and $ZnAlO_x$ catalysts (e.g., Zn:Cr ≈ 1:1 in the $ZnCrO_x$ system), the Zn content in $ZnZrO_x$ active catalysts can be extremely low. For instance, a $ZnZrO_x$ catalyst with a Zn:Zr ratio of 1:200 exhibits good catalytic selectivity (>60%) for converting syngas to methanol or DME over a wide temperature range (575–675 K) [139]. The pure ZrO_2/SSZ-13 catalyst yields very low syngas conversion activity (<5%). However, with just a 1.5% Zn addition, the activity increases to over 20%. Further increasing the Zn content to 5.9%, the CO conversion reaches 29% with 77% selectivity toward olefins [20]. Additionally, a $ZnZrO_x$ catalyst with a Zn content of 13% exhibits methanol selectivity ranging from 86% to 91% at a CO_2 conversion of more than 10% during CO_2 hydrogenation reactions [13]. These experiments suggest that even a minority presence of Zn could sufficiently activate CO_x/H_2. Therefore, it is imperative to elucidate the atomic structure and chemistry of $ZnZrO_x$ catalysts to better understand their catalytic behavior.

One perspective suggests that Zn is doped into the ZrO_2 lattice, leading to the formation of a $ZnZrO_x$ solid solution. Co-precipitation of zinc oxide and zirconia results in a material where zinc stabilizes the tetragonal phase of zirconia. Zirconia typically exhibits a monoclinic crystal structure at temperatures below 1170 °C, but the introduction of dopants is known to stabilize the metastable tetragonal structure. Several studies have observed a systematic shift in the (101) Bragg reflection to higher 2θ with increasing zinc loading until zirconia-zinc saturation is reached at approximately 33 mol% Zn [13,140]. This shift is caused by the substitution of Zr^{4+} (84 Å) with Zn^{2+} (74 Å), which shrinks the tetragonal lattice [141]. Additionally, FT-IR bands around 500 and 600–700 cm^{-1} are associated with Zn–O–Zn and Zn–O–Zr vibrations, respectively [142], and ultraviolet-visible (UV-vis) spectra of ZrO_2 change with the incorporation of Zn as a dopant [143]. Pérez-Ramírez and colleagues [144] prepared $ZnZrO_x$ catalysts using both flame spray pyrolysis (FSP) and coprecipitation (CP) methods. Catalysts synthesized via FSP systems (with up to 5 mol% Zn) exhibited three-fold higher methanol productivity compared to their CP counterparts. In-depth characterization and theoretical simulations revealed that, unlike CP, FSP maximizes the surface area and promotes the formation of atomically dispersed Zn^{2+} sites incorporated into lattice positions within the ZrO_2 surface.

Huang and colleagues [145] conducted a study where they prepared a series of ZnO-ZrO_2 composite oxides using the co-precipitation method. They observed that as the Zr content increased, the phase structures of the ZnO-ZrO_2 composite oxides evolved. Initially, they found a mixture of hexagonal ZnO phase and Zn-doped ZrO_2 solid solution phases. However, with increasing Zr content, the composite oxides transitioned to a pure Zn-doped ZrO_2 solid solution phase. This transformation was confirmed through metal content analysis using XPS and inductively coupled plasma (ICP) techniques (Figure 6a). Furthermore, they observed that the pure Zn-doped ZrO_2 solid solution phase exhibited high selectivity towards CH_3OH production, with bidentate formate species identified as the key intermediate. On the other hand, ZnO, tetragonal ZrO_2 (t-ZrO_2), monoclinic ZrO_2 (m-ZrO_2), and mixed-phased ZnO-ZrO_2 composite oxides displayed high selectivity towards CO production, with carbonates/bicarbonates species identified as the key intermediate (Figure 6b).

Feng et al. [146] investigated formate formation and conversion over the $ZnZrO_x$ solid solution catalyst using *in situ*/*operando* diffuse reflectance infrared Fourier transform spectroscopy-mass spectroscopy (DRIFTS-MS) coupled with DFT calculations. Their study revealed that bidentate carbonate, formed from CO_2 adsorption, is hydrogenated to formate on asymmetric Zn–O–Zr sites. In these sites, the Zn site facilitates H_2 activation, while the Zr site aids in stabilizing reaction intermediates. The asymmetric Zn–O–Zr sites, with adjacent and inequivalent features on the $ZnZrO_x$ catalyst, promote not only formate formation but also its transformation. DFT calculations based on the $ZnZrO_x$ solid solution model further validated the experimental results, confirming the existence of the $ZnZrO_x$ solid solution. These findings suggest that surface-available Zn^{2+} ions embedded in the zirconia crystal lattice, as part of a solid solution, in synergy with Zr^{4+} ions, constitute the active sites for CO_x hydrogenation.

Another perspective suggests that the Zn element predominantly exists in the form of ZnO supported on the ZrO_2

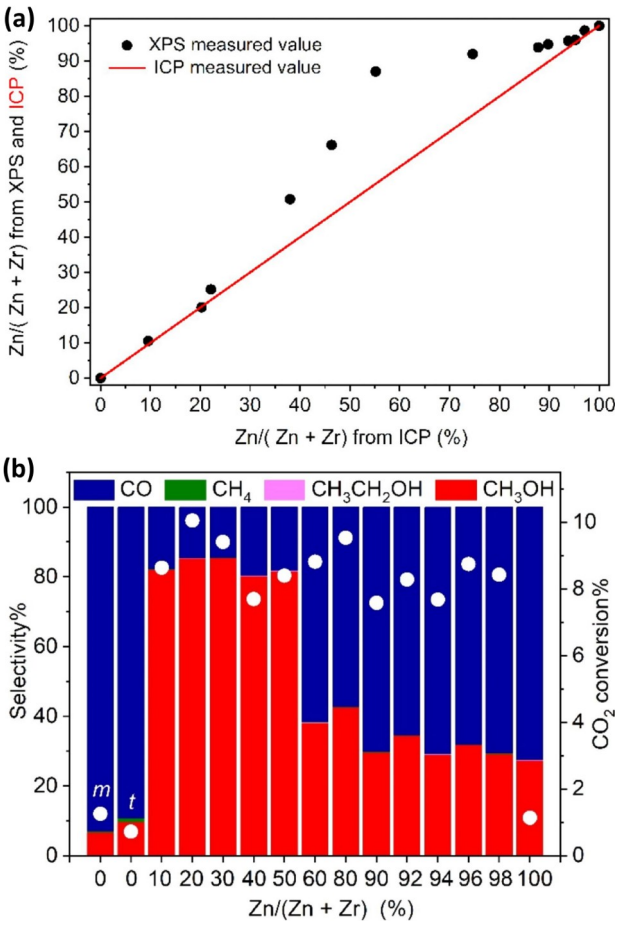

Figure 6 (Color online) The composition analysis and catalytic performance for $ZnZrO_x$ catalyst with different Zn:Zr ratio. (a) Zn/(Zn + Zr) ratios derived from XPS and ICP of ZnO-ZrO_2 composite catalyst as a function of those derived from ICP. (b) Steady-state CO_2 conversion (while sphere) and CO, CH_4, CH_3CH_2OH and CH_3OH selectivity of ZnO, ZrO_2 and ZnO-ZrO_2 composite oxides in CO_2 hydrogenation reaction at 593 K. Copyright with the permission of Elsevier from ref. [145].

surface. Due to the low content of Zn, the ZnO phase is challenging to detect by XRD. However, there is evidence supporting the formation of small ZnO clusters. X-ray absorption spectroscopy indicates low Zn–Zn or Zn–Zr coordination numbers, suggesting the presence of ZnO clusters [147]. Enrichment of Zn on the ZrO_2 surface detected by XPS implies that ZnO is predominantly located at the zirconia surface [148]. Even at low Zn content (Zn/Zr = 1/100), individual lattice fringes of isolated ZnO were observed by HRTEM, indicating the difficulty for Zn^{2+} to incorporate into the ZrO_2 lattice and a preference for the formation of separate ZnO phases [139]. *Ex/in situ* characterization techniques have demonstrated that Zn^{2+} species are mobile between the solid solution phase with ZrO_2 and segregated ZnO clusters [149]. Upon reductive heat treatments, partially reversible ZnO cluster growth occurs above 250 °C, with eventual Zn evaporation observed above 550 °C. Nikolajsen et al. [150] prepared co-precipitated ZnO-ZrO_2 catalysts and found that the initial activity correlated with the amount of amorphous ZnO on the support surface. They observed that catalytic activity increased with time on stream as zinc oxide migrated out of a solid solution with ZrO_2 and onto the support surface. Consequently, the active phase appeared to be ZnO surface species rather than zinc oxide in solid solution with ZrO_2.

Theoretically, through the utilization of machine learning (ML)-based large-scale atomistic simulation, we [151] investigated the PES of bulk $ZnZrO_x$ catalysts and discovered that the bulk structures of $ZnZrO_x$, regardless of Zn content, were consistently less stable than individual monoclinic ZrO_2 (m-ZrO_2) and ZnO, as evidenced by the positive bulk formation energy (Figure 7a). This observation suggests that $ZnZrO_x$ tends to segregate into ZnO and ZrO_2 biphases rather than forming a solid solution. Upon further exploration of surface biphase structures, the ZnO single layer on m-ZrO_2 (001) represents the most stable interface structure (Figure 7b). In this configuration, the Zn-O single layer facilitates high-temperature syngas conversion on the $ZnZrO_x$ system by stabilizing the key reaction intermediate CHO species. The highest occupied states exhibit salient difference between ZnO/m-ZrO_2 (001) and ZnO ($10\bar{1}0$). Compared to pure ZnO, ZnO/m-ZrO_2 have a much larger population of electrons and holes near Fermi level, as shown in Figure 7c, which would benefits the formation of key intermediate CHO species.

Setting aside the conflicting views, it is proposed that a Zn–O–Zr structural pattern serves as a common feature for both $ZnZrO_x$ solid solution and ZnO/ZrO_2 biphase, acting as the key catalytic site for CO_2 activation. Maximizing the number of Zn–O–Zr structural patterns may be crucial for enhancing catalytic performance. Building upon this concept, Zhang and colleagues [152] constructed Zn–O–Zr sites within a metal-organic framework (MOF) to gain insights into the structural requirements for methanol production. This catalyst exhibited over 99% methanol selectivity in CO_2 hydrogenation at 250 °C and achieved a high space-time yield of up to 190.7 $mg_{MeOH}\ g_{Zn}^{-1}\ h^{-1}$. Similarly, Lin et al. [153] prepared ZnO/ZrO_2 samples with various ZrO_2 polymorphic phases, including monoclinic, tetrahedral, and amorphous forms. Among these, amorphous ZrO_2, characterized by the largest surface area, was found to increase the Zn–O–Zr interface, resulting in the highest CO_2 conversion.

Additionally, enhancing the O_V content appears to be a common feature irrespective of whether considering the $ZnZrO_x$ solid solution or ZnO/ZrO_2 biphase views. *Operando* X-ray adsorption spectroscopy (XAS) coupled with modulation excitation spectroscopy revealed that the surface ZnO clusters were partly reduced under operating conditions, resulting in surface ZnO_x species with x approximately equal to 0.98 [150]. In the $ZnZrO_x$ solid solution catalyst, *in-situ*

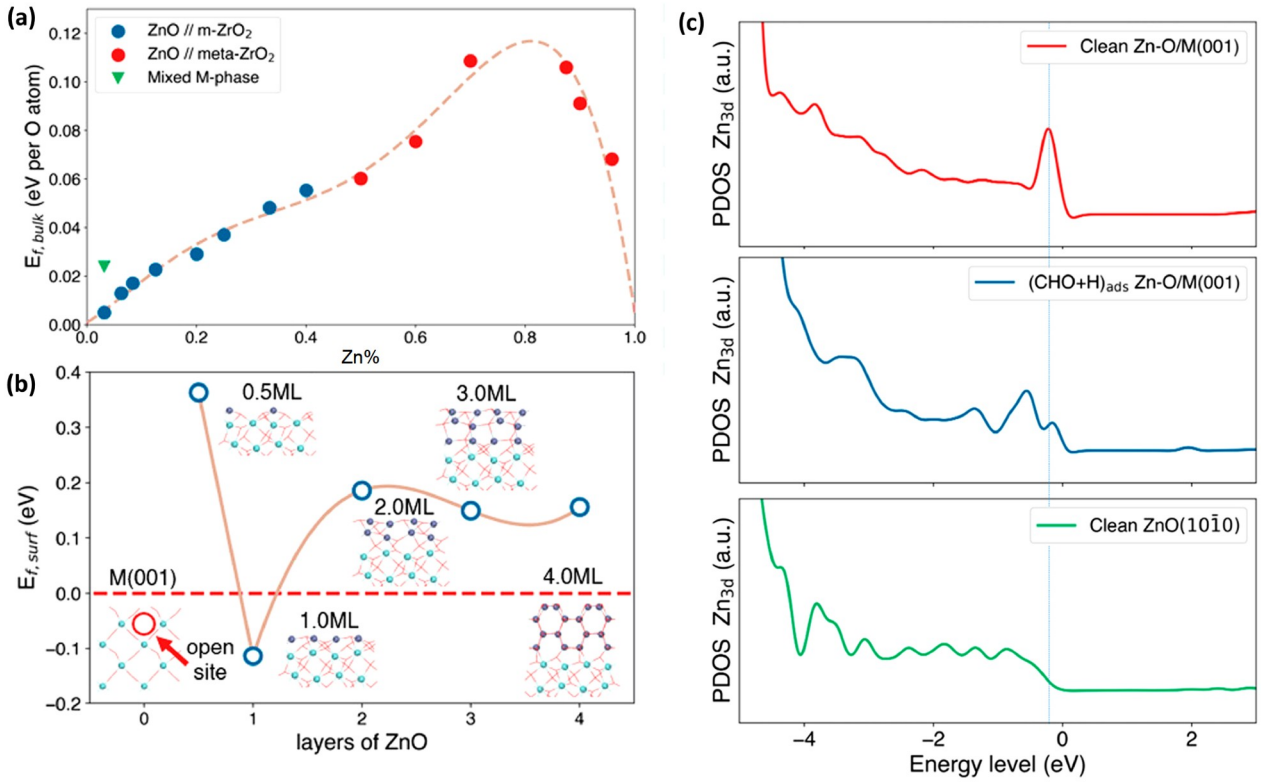

Figure 7 (Color online) Thermodynamic of $ZnZrO_x$ bulk phase and stable Zn–O single layer structures on ZrO_2 surfaces revealed by SSW-NN simulation. (a) Thermodynamic phase diagram of $ZnZrO_x$. (b) Formation energy ($E_{f,surf}$) of Zn–O on M(001) versus the thickness of ZnO. (c) PDOS onto the surface Zn 3d orbital for the clean Zn–O/m-ZrO_2(001) surface, CHO adsorbed Zn–O/m-ZrO_2(001) surface and the clean ZnO (10$\bar{1}$0) surface. Copyright with the permission of American Chemistry Society from ref. [151].

EPR spectroscopy confirmed the presence of O_V, where the signal intensity of these O_Vs was significantly stronger for the catalyst with the best CO_2 hydrogenation performance compared to other catalysts [144]. DFT calculation demonstrated that the Zn-doped ZrO_2 (101) surface exhibited negative O_V formation energy [154].

In summary, the surfaces of $ZnZrO_x$ catalysts likely expose Zn atoms in various local environments, depending on the preparation method. These environments may include individual Zn atoms substituted into the ZrO_2 matrix, Zn located on the surface and at the interface of nanoclustered ZnO, and Zn within larger segregated ZnO domains. Regardless of the form of Zn elements, both the Zn–O–Zr interface and the presence of O_V play pivotal roles in determining the catalytic performance. Hence, finely tuning these factors is crucial for optimizing catalytic activity.

3 Reaction mechanism of CO_x hydrogenation on Zn-based mixed oxide catalyst

3.1 CO hydrogenation mechanism

Syngas conversion on Fe- and Co-based metal catalysts typically follows the carbon chain growth mechanism, resulting in the presence of Anderson-Schulz-Flory (ASF) distributions. In contrast, on Zn-based catalysts, a completely different CO hydrogenation mechanism is observed. On a pure ZnO surface, the formation of $HCOO^-$ has been confirmed through ambient pressure XPS, evidenced by the appearance of a C 1s peak at 289.9 eV at 400 K. The formation of the $HCOO^-$ species involves both the oxidation of CO and the hydrogenation process, with the lattice oxygen of ZnO believed to participate in the formation of $HCOO^-$. DFT calculations have confirmed that the formation of $HCOO^-$ is thermodynamically preferred, with an accessible formation energy barrier of 1.06 eV (Figure 8a) [155].

On the $ZnCrO_x$ catalyst, our previous work [127] proved that the CO hydrogenation on $ZnCrO_x$ catalysts follows the stepwise hydrogenation mechanism, CO → CHO → CH_2O→ CH_3O → CH_3OH/CH_4. In this mechanism, the rate-determining step (RDS) is the hydrogenation of CH_3O step, which also determines the selectivity of CH_3OH or CH_4 (Figure 9a). On the reduced $Zn_3Cr_3O_8$ surface, the reaction channel leading to CH_3OH is kinetically much more facile, with a reaction barrier of 1.33 eV, whereas the formation of CH_4 has a significant reaction barrier of 2.41 eV. The calculated reaction barrier for methanol formation on the $Zn_3Cr_3O_8$ surface aligns well with the experimental observed

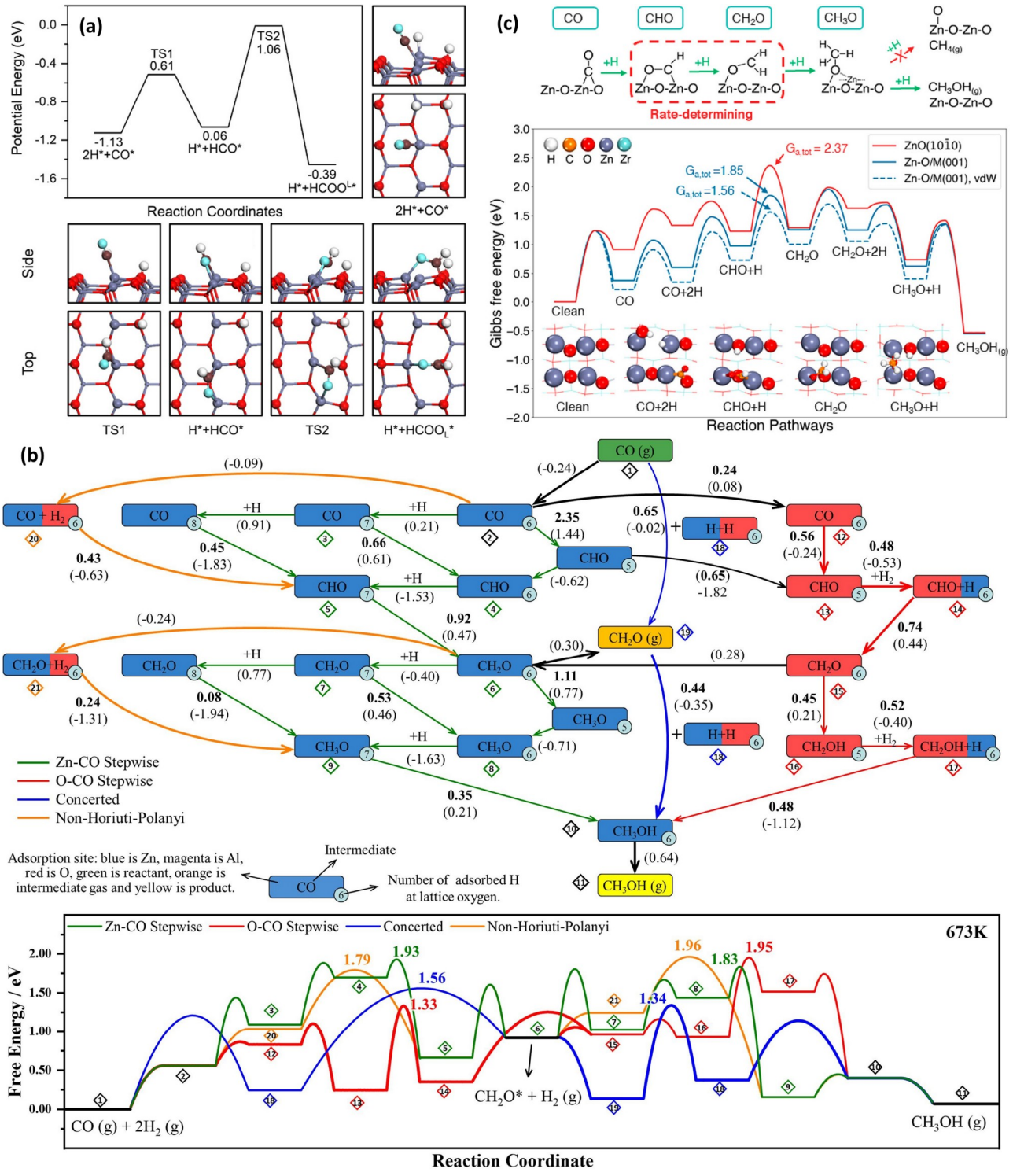

Figure 8 (Color online) The CO hydrogenation mechanism on different Zn-based catalysts. (a) Potential energy surface and intermediate configurations and transition state configurations of CO hydrogenation to HCOO* on the stoichiometric ZnO(10$\bar{1}$0) surface. Gray, red, green, brown, and white spheres represent Zn, lattice O, O in adsorbates, C atoms, and H atoms, respectively. Copyright with permission from American Chemistry Society from ref. [155]. (b) Calculated Gibbs free energy diagram of syngas-to-methanol via different reaction pathways on $ZnAl_2O_4$ (111) surface. Copyright with permission of Elsevier from ref. [136]. (c) Gibbs free energy profile of syngas conversion on single layer ZnO on m-ZrO_2 (001) (Zn–O/M(001)) and ZnO(10$\bar{1}$0) at 673 K and 3 MPa (H_2:CO = 2:1). The key reaction intermediates on Zn–O/M(001) and the mechanism are also depicted. Copyright with permission of American Chemistry Society from ref. [151].

apparent activation energy of ~1.20 eV (113 ± 5 kJ mol^{-1}) reported by Errani et al. [124].

When the $ZnCrO_x$ coupled with zeolite, CH_2CO (ketene) was detected and considered a possible intermediate [8]. Hu

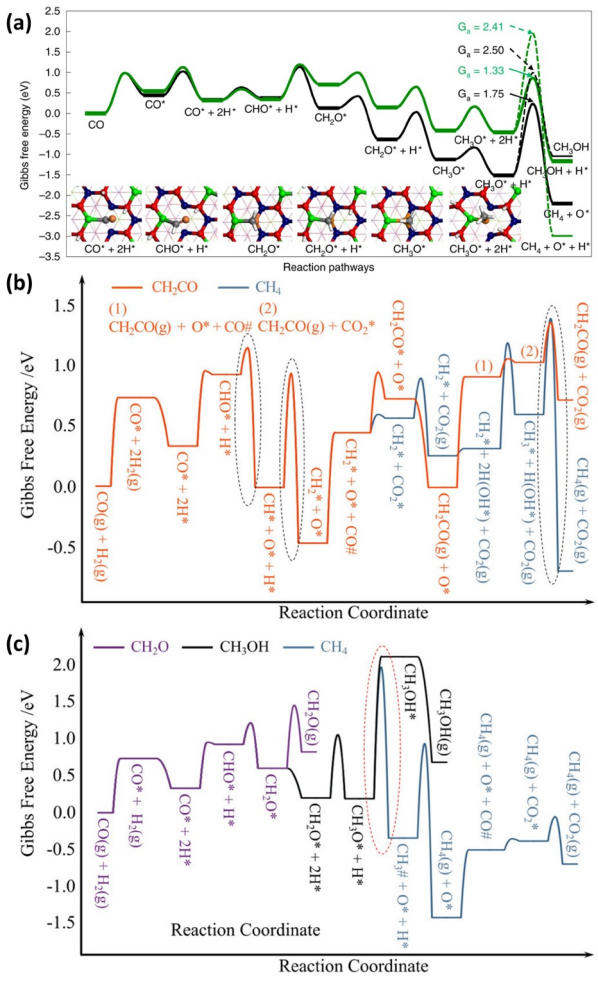

Figure 9 (Color online) (a) Gibbs free energy reaction profiles for syngas conversion rates on reduced $ZnCr_2O_4$ (111) and $Zn_3Cr_3O_8$ (0001) surfaces at 573 K and 2.5 MPa syngas (H_2:CO = 1.5). The black and green lines represent the reduced $ZnCr_2O_4$ (111) and $Zn_3Cr_3O_8$ (0001) surfaces, respectively. The asterisk indicates the adsorption state. The reaction snapshots are shown in the inset of (a): Zn, green; Cr, purple; O, red; O in CO, orange. C, grey; H, white. Copyright with permission of Nature from ref. [127]. (b, c)The energy profiles of the formation of (b) CH_2CO and CH_4, and (c) CH_2O, CH_3OH, and CH_4 on reduced $ZnCr_2O_4$(110) surface. The rate-limiting steps of the formation of CH_2CO and CH_3OH are circled by the black and red dotted lines, respectively. Copyright with permission of American Chemistry Society from ref. [129].

and co-workers [129] performed systematic DFT calculations and microkinetic simulations to inspect the possible elementary steps on the highly reduced $ZnCr_2O_4$(110) surface, which quantitatively unveiled the favored reaction pathways for CO activation and conversion. As shown in Figure 9b, c, the conversion of CHO played a vital role in product selectivity; the dissociation of CHO was identified to proceed easily and constituted a major route responsible for the formation of CH_4 and CH_2CO through the following pathway: CHO → CH + O; CH + H → CH_2; CH_2 + CO → CH_2CO; or CH_2 + 2H → CH_4. Alternatively, CHO could undergo hydrogenation to give CH_2O and CH_3O intermediates, eventually leading to the formation of CH_3OH and CH_4. The kinetic analyses on such a complex reaction network disclosed that CH_4 is the dominant product, while both CH_2CO and CH_3OH (i.e., two experimentally controversial intermediates) exist in minority, with CH_2CO being relatively more readily formed. The kinetic model illustrated that the selectivity for CH_2CO and the formation of triggered light olefins can be significantly improved over CH_4 if a reaction channel converts CH_2CO to light olefins when zeolite is added. This provides insight into the bifunctionality of the oxide/zeolite system.

Wang and co-workers [136] investigated the reaction pathways for syngas-to-methanol on $ZnAl_2O_4$ spinel oxide surfaces. They considered four dominant reaction pathways: Zn-CO stepwise, O-CO stepwise, concerted and Non-Horiuti-Polanyi pathways. In the stepwise pathway, carbon-containing species adsorb on metal (Zn-CO) or oxygen (O-CO) sites, and the adsorbed hydrogen atom participates in the reaction in a stepwise manner. In the concerted pathway, a H_2 molecule fist heterolytically dissociates on O-Zn sites, and then CO or CH_2O directly reacts with proton and hydride simultaneously. The Non-Horiuti-Polanyi pathway involves the participation of H_2 molecule from gas-phase for the first hydrogenation of CO or CH_2O. They revealed that $ZnAl_2O_4$ (111) is the active surface for syngas conversion. The O-CO stepwise pathway (1.33 eV) is most favored in the hydrogenation of CO to CH_2O process, followed by the concerted pathway (1.56 eV), the Non-Horiuti-Polanyi pathway (1.79 eV), and the Zn-CO stepwise pathway (1.93 eV) (Figure 8b). Under typical simulation conditions of a total pressure of 3 MPa and H_2/CO = 1, the maximum overall reaction rate is calculated to be ~13 s^{-1} at ~628 K, agreeing well with the reaction rate calculated under the experimental conditions (~20 s^{-1} at ~643 K) at the same 8% CO conversion [18,59]. The apparent activation energy of syngas-to-methanol on $ZnAl_2O_4$(111) surface is theoretically deduced to be ~79 kJ mol^{-1}, fitting within a temperature range of 473–773 K, which is similar with the experimental data of 87 kJ mol^{-1} for syngas-to-methanol conversion on $ZnAl_2O_4$ [156].

Our previous work [151] explored possible reaction pathways for syngas-to-methanol on a ZnO(10$\bar{1}$0) surface, revealing a stepwise hydrogenation pathway mediated by CHO, CH_2O, and CH_3O (CO → CHO → CH_2O → CH_3O → CH_3OH), as shown in Figure 8c. However, the total reaction energy barrier was found to be much higher (2.1 eV), suggesting that the ZnO surface is inert for syngas conversion, consistent with experimental observations. In contrast, a single layer of ZnO supported on the m-ZrO_2 (001) surface (Zn–O/M(001)), representative of the $ZnZrO_x$ catalyst, catalyzes syngas conversion with a dramatically decreased reaction barrier of 1.56 eV. Microkinetic analysis yielded an apparent activation energy of 83 kJ mol^{-1}, which aligns well

with experimental values of 72 ± 5 kJ mol^{-1} on the $ZnZrO_x$ (Zn% = 1/16) catalyst [20].

3.2 CO_2 hydrogenation mechanism

Generally speaking, there are two main routes for CO_2 hydrogenation to methanol. The first one is the formate pathway, where CO_2 reacts with the pre-adsorbed surface atomic hydrogen to form formate (HCOO) via either an Eley-Rideal or Langmuir-Hinshelwood mechanism. The formate species is further hydrogenated to dioxomethylene (H_2COO*), formaldehyde (H_2CO*), methoxy (CH_3O*), and finally methanol (CH_3OH*). The other one is the RWGS + CO-hydro pathway, where CO_2 is first converted to CO via the carboxyl (COOH*) intermediate or direct dissociation. It is then hydrogenated to methanol via the formyl (HCO*), formaldehyde (H_2CO*), and methoxy (H_3CO*) intermediates. In the CO_2 hydrogenation process, the key elementary step is the breaking of the C–O bond.

On ZnO($10\bar{1}0$) surface, exposure to CO_2 leads to the formation of surface carbonate species, which has been confirmed by near-edge X-ray absorption fine structure (NEXAFS) [158] and HREELS studies [159]. DFT calculations [159] suggested that the optimal adsorbate structure for CO_2 manifests as a tridentate configuration. In this configuration, the carbon atom forms a bond with a surface threefold coordinated O site, and both oxygen atoms in CO_2 interact with adjacent threefold coordinated Zn sites. Upon elevating the temperature, ambient pressure (AP)-syngas-to-methanol and AP-XPS measurements [155] showed the formation of formate species, pointing to the transformation of CO_2 to formate. DFT calculations indicated that formate species can easily form through the reaction of CO_2 with a hydride bonded to the surface Zn_{3c} site, with the energy barrier of only 0.3 eV. Zhao et al. [157] found that the formations of both $HCOO^-$ and CO_3^{2-} species on the perfect ZnO(0001) surface are spontaneous upon exposure to a CO_2 and H_2 mixture (Figure 10a). Since both $HCOO^-$ and CO_3^{2-} are very stable on the surface, their further conversion to other reaction intermediates is extremely difficult. This leads to the accumulation of both $HCOO^-$ and CO_3^{2-} species, explaining why these species are typically observed on ZnO catalyst surfaces in experiments. Similar results have also been reported by Medford et al. [160].

On Zn-based mixed oxides surfaces, these steps proceed readily due to the presence of new metal sites and surface O_Vs, as one oxygen atom from CO_2 or its hydrogenation intermediates will replenish the surface vacancy during the conversion. CO_3^{2-}, HCO_3^-, HCOO* and CH_3O* species are identified on $ZnCrO_x$ surface by several groups utilizing *in-situ* DRIFTS [71–73,75]. Similarly, the signal of HCOO* and CH_3O* species are observed by *operando* DRIFTS and FT-IR on $ZnAl_2O_4$ catalyst surface [11,18].

For the $ZnZrO_x$ catalyst, Wang et al. [13] performed the *in-situ* DRIFTS and DFT calculation to understand the reaction mechanisms of CO_2 hydrogenation on $ZnZrO_x$ solid solution catalyst. *In situ* DRIFTS results show that the surface HCOO* and H_3CO* species on the ZnO-ZrO_2 solid solution catalyst can be hydrogenated to methanol. DFT calculations reveal that CO_2 hydrogenation to methanol on the surface of ZnO-ZrO_2 follows the formate pathway rather than the CO pathway, as illustrated in Figure 10b. In this pathway, H_2 is adsorbed and dissociated on the Zn site, while CO_2 is adsorbed on the coordination unsaturated Zr site. The CO_2* transforms into HCOO* species via hydrogenation. These HCOO* species are further hydrogenated to the H_2COO* species, which are then protonated by an OH* group and form H_2COOH* species. The C–O bond in H_2COOH* is

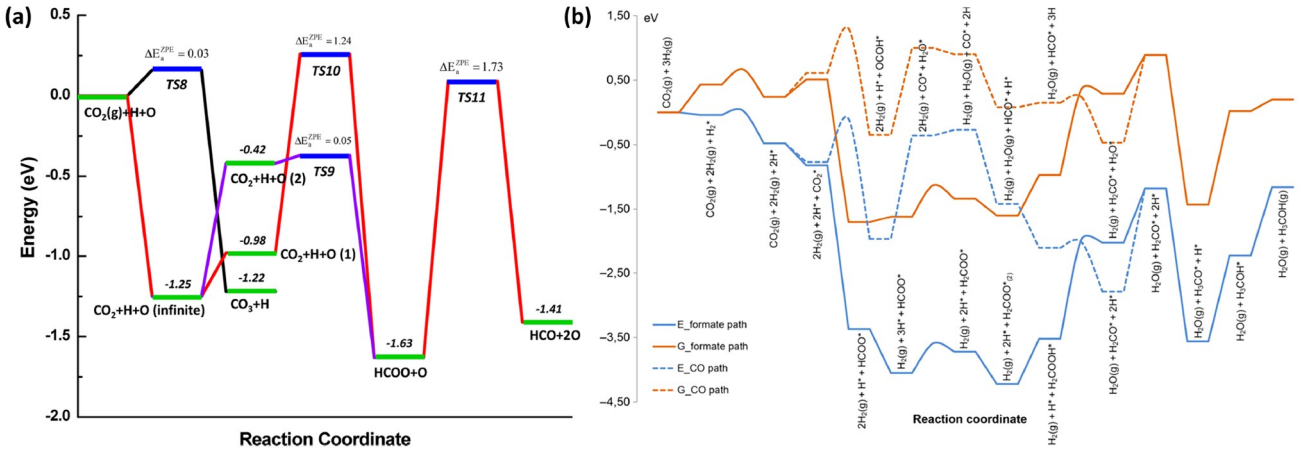

Figure 10 (Color online) (a) CO_2 hydrogenation and dissociation on the ZnO(0001) surface. The activation barriers listed in the figure include zero point energy (ZPE) corrections. Copyright with permission of American Chemistry Society of ref. [157]. (b) Reaction diagram (energy (*E*) and Gibbs free energy (*G*) at a typical reaction temperature of 593 K) of CO_2 hydrogenation to methanol on the (101) surface of the tetragonal ZnO-ZrO_2 model. Copyright with permission from American Association for the Advancement of Science of ref. [13].

cleaved, generating H_2CO^* and OH* bound on Zr and Zn sites, respectively. The generated H_2CO^* is hydrogenated to H_3CO^*, and methanol forms from the protonation of H_3CO^*. Conversely, in the CO pathway, COOH* is much less stable than HCOO*, requiring a large barrier of 0.69 eV to form, which is unfavorable compared to the barrier-less process of $CO_2^* + H^* \rightarrow HCOO^*$. Similar results were also obtained on the reduced $ZnZrO_x$ solid solution surface [154].

4 Summary and outlook

The catalytic synthesis of valuable hydrocarbons via CO_x hydrogenation represents an important, non-petroleum route towards future clean-energy society. The Zn-based oxide catalysts have emerged as one of the most important candidates for such synthesis. Continuous efforts have been devoted to searching for new elements and materials to tune CO_x and H_2 adsorption and activation, and invent new catalyst preparation methods to address catalytic activity and long-term stability.

Although debates persist regarding the exact nature of the catalytic active sites in various Zn-based mixed oxides, certain consensuses have been reached in the past years. For instance, the concentration of O_V and the excess Zn in ZnM_2O_4 (M = Zn, Al) and ZrO_2 are two significant catalytic descriptors for future catalyst design. The Zn-based oxides are prone to partial removal of lattice oxygen and the formation of O_Vs during calcination or reduction processes. These O_Vs, with unpaired electrons, can weaken C–O bonds and enhance the adsorption of CO_x [127,130,136,151]. The exposed active structures of Zn-based oxides do differ in the CO and CO_2 hydrogenation due to the distinct reductive abilities of CO and H_2. Specifically, in CO hydrogenation, CO has a much stronger reductive ability compared to H_2, resulting in a higher concentration of O_Vs on the Zn-based oxide surfaces [127]. In contrast, during CO_2 hydrogenation, only H_2 is available in reducing the oxide surface and as a result, the O_V concentration is significantly lower. This difference in O_V concentration directly affects the catalytic activity and the reaction mechanisms involved. Although increasing the concentration of O_Vs has been shown to enhance reaction activity, conflicting studies suggest that a too high surface O_V concentration may actually reduce reaction activity and product selectivity [161,162]. Therefore, further *operando* research is needed to elucidate the impact of the O_V concentration under experimental reaction conditions. For example, for the $Zn_3Cr_3O_8$ spinel phase at room temperature and vacuum conditions, only the surface O_V can be formed with a concentration of 0.25 monolayer. At this concentration, the metal site is inert for the syngas-to-methanol reaction. However, under reaction conditions, besides the surface O_V, the subsurface O_V with a concentration of 0.25 monolayer also forms, leading to the creation of the real active site for the syngas-to-methanol reaction [127]. Therefore, although the surface science (low pressure) characterization can provide valuable insights into the surface properties, one must bear in mind that dramatic structure difference may occur under realistic reaction conditions.

Moreover, the atomic configuration and valence state of the extra Zn are not yet well understood. In particular, there is a lack of a quantitative metric to evaluate the interaction between extra Zn and different supports. Questions remain about when and how Zn incorporates into the lattice matrix of supports and Zn forms strong metal-support interactions (SMSI), which is critical to control the catalyst synthesis and guide the activity optimization.

For the reaction mechanism, CO_x hydrogenation on different Zn-based mixed oxides follows very similar reaction pathways but exhibits different reaction rates. As above mentioned, the CO conversion rate can reach 80% on $ZnCrO_x$, while it is lower on $ZnAlO_x$ and $ZnZrO_x$. This abnormal variation in reaction rates and activation energies is attributed to differences in the reaction profile types. By comparing the free energy profiles on different catalysts, we can categorize these reactions into two types: early-RDS and late-RDS types. The early-RDS type refers to situations where the RDS occurs in the first half of the reaction curve relating to the reactant activation, whereas the late-RDS type refers to the RDS occurring in the latter half on the product release (Figure 11). The weak interaction between Zn, Al, and Zr with CO leads to early-RDS curves for ZnO, $ZnAlO_x$, and $ZnZrO_x$ systems, with the apparent activation energy in the range of 80–90 kJ mol^{-1} [136,151]. In contrast, the strong interaction between Cr and CO results in a late-RDS curve for the $ZnCrO_x$ system, with the apparent activation energy exceeding 110 kJ mol^{-1} [124]. According to microkinetic simulations, the free energy barrier for the early-RDS curves could include the entropy loss during the adsorption and activation of the reactant molecule, which is temperature dependent and not reflected in the apparent activation energy. Therefore, the early-RDS curves may exhibit lower apparent activation energies. In contrast, the energy barrier for the late-RDS curves relates to the formation of reaction intermediates and products, which are generally surface recombination reactions and it is usually consistent with the apparent activation energy. Therefore, a low apparent activation energy is not necessarily associated with a high reaction rate. To further improve catalytic activity, it is beneficial to balance the two types of reaction profiles, which might be achievable by mixing two types of materials to generate the optimal reaction curve.

Considering the great structural complexity of mixed oxide system and the high temperature nature of these catalytic processes, it is no wonder that many questions remain on the nature of the active site and their interplay with the catalytic

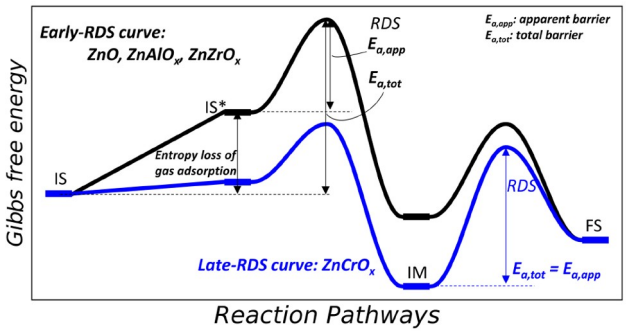

Figure 11 (Color online) The early-RDS and late-RDS types free energy profiles for Zn-based oxide catalysts.

activity and selectivity. These questions provide a concrete handle to probe these mixed oxide systems via improving scientific instruments, and will certainly guide the future research to design better oxide catalysts to achieve CO_x hydrogenation with high activity and selectivity.

Acknowledgements This work was supported by the National Natural Science Foundation of China (12188101, 91745201, 91945301, 22203101, and 22033003), the Fundamental Research Funds for the Central Universities (20720220011), the Youth Innovation Promotion Association CAS (2023265), the Science & Technology Commission of Shanghai Municipality (23ZR1476100), and the Tencent Foundation for EXPLORER PRIZE.

Conflict of interest The authors declare no conflict of interest.

1 Zhang X, Zhang G, Song C, Guo X. *Front Energy Res*, 2021, 8: 621119
2 Schwartz SE. *Energy Environ Sci*, 2008, 1: 430
3 Abanades JC, Rubin ES, Mazzotti M, Herzog HJ. *Energy Environ Sci*, 2017, 10: 2491–2499
4 Zhou W, Cheng K, Kang J, Zhou C, Subramanian V, Zhang Q, Wang Y. *Chem Soc Rev*, 2019, 48: 3193–3228
5 Cui WG, Zhang GY, Hu TL, Bu XH. *Coord Chem Rev*, 2019, 387: 79–120
6 Bao J, Yang G, Yoneyama Y, Tsubaki N. *ACS Catal*, 2019, 9: 3026–3053
7 Chang X, He M, Lu Q, Xu B. *Sci China Chem*, 2023, 66: 96–106
8 Jiao F, Li J, Pan X, Xiao J, Li H, Ma H, Wei M, Pan Y, Zhou Z, Li M, Miao S, Li J, Zhu Y, Xiao D, He T, Yang J, Qi F, Fu Q, Bao X. *Science*, 2016, 351: 1065–1068
9 Zhou W, Cheng K, Zhang Q, Wang Y. *Chin Sci Bull*, 2021, 66: 1157–1169
10 Li Z, Wang J, Qu Y, Liu H, Tang C, Miao S, Feng Z, An H, Li C. *ACS Catal*, 2017, 7: 8544–8548
11 Ni Y, Chen Z, Fu Y, Liu Y, Zhu W, Liu Z. *Nat Commun*, 2018, 9: 3457
12 Wei J, Ge Q, Yao R, Wen Z, Fang C, Guo L, Xu H, Sun J. *Nat Commun*, 2017, 8: 15174
13 Wang J, Li G, Li Z, Tang C, Feng Z, An H, Liu H, Liu T, Li C. *Sci Adv*, 2017, 3: e1701290
14 Chen K, Wang F, Wang Y, Zhang F, Huang X, Kang J, Zhang Q, Wang Y. *JACS Au*, 2023, 3: 2894–2904
15 Wang W, Zeng C, Tsubaki N. *Green Carbon*, 2023, 1: 133–145
16 Xiong WT, Wu G, Chen SC, Wang YZ. *Sci China Chem*, 2023, 66: 2062–2069
17 Deng B, Zhao X, Li Y, Huang M, Zhang S, Dong F. *Sci China Chem*, 2023, 66: 78–95
18 Liu X, Wang M, Yin H, Hu J, Cheng K, Kang J, Zhang Q, Wang Y. *ACS Catal*, 2020, 10: 8303–8314
19 Ni Y, Liu Y, Chen Z, Yang M, Liu H, He Y, Fu Y, Zhu W, Liu Z. *ACS Catal*, 2019, 9: 1026–1032
20 Liu X, Zhou W, Yang Y, Cheng K, Kang J, Zhang L, Zhang G, Min X, Zhang Q, Wang Y. *Chem Sci*, 2018, 9: 4708–4718
21 Wei J, Yao R, Ge Q, Wen Z, Ji X, Fang C, Zhang J, Xu H, Sun J. *ACS Catal*, 2018, 8: 9958–9967
22 Gao P, Li S, Bu X, Dang S, Liu Z, Wang H, Zhong L, Qiu M, Yang C, Cai J, Wei W, Sun Y. *Nat Chem*, 2017, 9: 1019–1024
23 Gao P, Dang S, Li S, Bu X, Liu Z, Qiu M, Yang C, Wang H, Zhong L, Han Y, Liu Q, Wei W, Sun Y. *ACS Catal*, 2018, 8: 571–578
24 Jiao F, Pan X, Gong K, Chen Y, Li G, Bao X. *Angew Chem Int Ed*, 2018, 57: 4692–4696
25 Li G, Jiao F, Pan X, Li N, Miao D, Li L, Bao X. *ACS Catal*, 2020, 10: 12370–12375
26 Molstad MC, Dodge BF. *Ind Eng Chem*, 1935, 27: 134–140
27 Sha F, Tang S, Tang C, Feng Z, Wang J, Li C. *Chin J Catal*, 2023, 45: 162–173
28 John Thomas G, John Mitchell K. Methanol synthesis. British patent. GB1159035A, 1966-07-26
29 Phineas D, Frederick Forster S. Production of oxygenated hydrocarbons. US patent. US3326956A, 1963-06-03
30 Liu XM, Lu GQ, Yan ZF, Beltramini J. *Ind Eng Chem Res*, 2003, 42: 6518–6530
31 Chang C. *J Catal*, 1977, 47: 249–259
32 Kianfar E, Hajimirzaee S, mousavian S, Mehr AS. *MicroChem J*, 2020, 156: 104822
33 Tian P, Wei Y, Ye M, Liu Z. *ACS Catal*, 2015, 5: 1922–1938
34 Yang M, Fan D, Wei Y, Tian P, Liu Z. *Adv Mater*, 2019, 31: 1902181
35 Fu T, Guo Y, Li Z, Zhan G. *Fuel*, 2022, 315: 123241
36 Wang Y, Li T, Ouyang Y, Zhong J, Zhang Y, Xiong X, Hu Q, Deng J, Sun H, Yan Z. *Catal Sci Technol*, 2024, 14: 2461–2469
37 Zhang J, Zhu X, Zhang S, Cheng M, Yu M, Wang G, Li C. *Catal Sci Technol*, 2019, 9: 316–326
38 Fathi S, Sohrabi M, Falamaki C. *Fuel*, 2014, 116: 529–537
39 Yang M, Li B, Gao M, Lin S, Wang Y, Xu S, Zhao X, Guo P, Wei Y, Ye M, Tian P, Liu Z. *ACS Catal*, 2020, 10: 3741–3749
40 Zou X, Fan D, Zhang X, Lou C, Yang M, Xu S, Wang Q, Tian P, Liu Z. *Chem Commun*, 2024, 60: 4805–4809
41 Cheng K, Gu B, Liu X, Kang J, Zhang Q, Wang Y. *Angew Chem Int Ed*, 2016, 55: 4725–4728
42 Fujimoto K, Saima H, Tominaga H. *Ind Eng Chem Res*, 1988, 27: 920–926
43 Jiao F, Bai B, Li G, Pan X, Ye Y, Qu S, Xu C, Xiao J, Jia Z, Liu W, Peng T, Ding Y, Liu C, Li J, Bao X. *Science*, 2023, 380: 727–730
44 Kung HH. *Catal Rev*, 1980, 22: 235–259
45 Piero GD, Trifiro F, Vaccari A. *J Chem Soc Chem Commun*, 1984, 656–658
46 Tan L, Wang F, Zhang P, Suzuki Y, Wu Y, Chen J, Yang G, Tsubaki N. *Chem Sci*, 2020, 11: 4097–4105
47 Jin D, Meng X, Gao W, Xu B, Dai W, Zhao R, Xu F, Yang D, Xin Z. *Ind Eng Chem Res*, 2023, 62: 211–222
48 Jin D, Xin Z, Meng X, Dai W, Xu B, Zhao R, Xu F, Yang D. *Chem Eng J*, 2024, 480: 147593
49 Wei X, Yuan L, Li W, Chen S, Liu Z, Cheng S, Li L, Wang C. *Catal Lett*, 2023, 153: 3433–3441
50 Ding Y, Jiao F, Pan X, Ji Y, Li M, Si R, Pan Y, Hou G, Bao X. *ACS Catal*, 2021, 11: 9729–9737
51 Wang X, Cao R, Chen K, Si C, Ban H, Zhang P, Meng F, Jia L, Mi J, Li Z, Li C. *ChemCatChem*, 2020, 12: 4387–4395
52 Huang Y, Ma H, Xu Z, Qian W, Zhang H, Ying W. *ACS Omega*, 2021, 6: 10953–10962
53 Su J, Zhou H, Liu S, Wang C, Jiao W, Wang Y, Liu C, Ye Y, Zhang L, Zhao Y, Liu H, Wang D, Yang W, Xie Z, He M. *Nat Commun*, 2019, 10: 1297

54 Huang Y, Ma H, Xu Z, Qian W, Zhang H, Ying W. *RSC Adv*, 2021, 11: 13876–13884
55 Su J, Liu C, Liu S, Ye Y, Du Y, Zhou H, Liu S, Jiao W, Zhang L, Wang C, Wang Y, Xie Z. *Cell Rep Phys Sci*, 2021, 2: 100290
56 Wang Z, Wei Y, Qi J, Wan J, Wang Z, Yu R, Wang D. *Adv Funct Mater*, 2024, 34: 2316547
57 Pan X, Jiao F, Miao D, Bao X. *Chem Rev*, 2021, 121: 6588–6609
58 Jiao W, Su J, Zhou H, Liu S, Liu C, Zhang L, Wang Y, Yang W. *Microporous Mesoporous Mater*, 2020, 306: 110444
59 Zhou W, Kang J, Cheng K, He S, Shi J, Zhou C, Zhang Q, Chen J, Peng L, Chen M, Wang Y. *Angew Chem Int Ed*, 2018, 57: 12012–12016
60 Ding Y, Miao D, Feng J, Bai B, Pan X, Bao X. *Appl Catal B-Environ*, 2022, 316: 121628
61 Ding Y, Zhao Y, Miao D, Wang Z, Feng J, Jiao F, Pan X, Bao X. *J Phys Chem C*, 2024, 128: 4508–4515
62 Ding Y, Miao D, Wang Z, Feng J, Zhang P, Yu R, Cao X, Pan X, Bao X. *ACS Catal*, 2023, 13: 14277–14284
63 Chang C. *J Catal*, 1979, 56: 268–273
64 Ereña J, Arandes JM, Bilbao J, Aguayo AT, de Lasa HI. *Ind Eng Chem Res*, 1998, 37: 1211–1219
65 Tian G, Liu X, Zhang C, Fan X, Xiong H, Chen X, Li Z, Yan B, Zhang L, Wang N, Peng HJ, Wei F. *Nat Commun*, 2022, 13: 5567
66 Fu Y, Ni Y, Chen Z, Zhu W, Liu Z. *J Energy Chem*, 2022, 66: 597–602
67 Ma Z, Wang X, Ma X, Tan M, Yang G, Tan Y. *Microporous Mesoporous Mater*, 2023, 349: 112420
68 Fu Y, Ni Y, Cui W, Fang X, Chen Z, Liu Z, Zhu W, Liu Z. *Green Energy Environ*, 2023, 8: 530–537
69 Ma Z, Tan M, Cao F, Yang Y, Gong N, Wu Y, Zhang J, Yang G, Tan Y. *AIChE J*, 2023, 69: e17979
70 Ma Z, Cao F, Yang Y, Wang L, Zhang T, Tan M, Yang G, Tan Y. *Fuel*, 2022, 325: 124809
71 Gao W, Guo L, Cui Y, Yang G, He Y, Zeng C, Taguchi A, Abe T, Ma Q, Yoneyama Y, Tsubaki N. *ChemSusChem*, 2020, 13: 6541–6545
72 Arslan MT, Tian G, Ali B, Zhang C, Xiong H, Li Z, Luo L, Chen X, Wei F. *ACS Catal*, 2022, 12: 2023–2033
73 Zhang J, Zhang M, Chen S, Wang X, Zhou Z, Wu Y, Zhang T, Yang G, Han Y, Tan Y. *Chem Commun*, 2019, 55: 973–976
74 Miao D, Pan X, Jiao F, Ji Y, Hou G, Xu L, Bao X. *Catal Sci Technol*, 2021, 11: 4521–4528
75 Guo S, Fan S, Wang H, Wang S, Qin Z, Dong M, Fan W, Wang J. *ACS Catal*, 2024, 14: 271–282
76 Shi Y, Gao W, Wang G, Fan J, Wang C, Wang F, He Y, Guo X, Yasuda S, Yang G, Tsubaki N. *Mater Today Chem*, 2023, 32: 101654
77 Guo S, Wang S, Zhang W, Wang H, Zhang Q, Qin Z, Dong M, Wang J, Fan W. *Ind Eng Chem Res*, 2022, 61: 10409–10418
78 Raveendra G, Li C, Cheng Y, Meng F, Li Z. *New J Chem*, 2018, 42: 4419–4431
79 Ren L, Zhang J, Wang B, Xu H, Jiang J, Guan Y, Wu P. *Fuel*, 2022, 307: 121916
80 Wang Y, Wang G, van der Wal LI, Cheng K, Zhang Q, de Jong KP, Wang Y. *Angew Chem Int Ed*, 2021, 60: 17735–17743
81 Meng F, Li B, Zhang J, Wang L, Li Z. *Fuel*, 2023, 346: 128351
82 Li B, Meng F, Wang L, Li Z. *J Fuel Chem Tech*, 2023, 51: 111–119
83 Su J, Zhang L, Zhou H, Ye Y, Zheng X, Liu C, Liu S, Jiao W, Liu X, Wang C, Wang Y, Xie Z. *ACS Catal*, 2023, 13: 2472–2481
84 Zhang Z, Huang Y, Ma H, Qian W, Zhang H, Ying W. *Catal Commun*, 2021, 152: 106292
85 Liu S, Liu J, Chen G, Yao J, Yan B, Yi W, Cheng Z, Tian C, Zao H. *Fuel Processing Tech*, 2023, 252: 107967
86 Fang Y, Sheng H, Huang Z, Yue Y, Hua W, Shen W, Xu H. *ChemCatChem*, 2022, 14: e202200200
87 Wang S, Wang P, Shi D, He S, Zhang L, Yan W, Qin Z, Li J, Dong M, Wang J, Olsbye U, Fan W. *ACS Catal*, 2020, 10: 2046–2059
88 Raveendra G, Li C, Liu B, Cheng Y, Meng F, Li Z. *Catal Sci Technol*, 2018, 8: 3527–3538
89 Zhang Q, Li X, Asami K, Asaoka S, Fujimoto K. *Fuel Processing Tech*, 2004, 85: 1139–1150
90 Li N, Jiao F, Pan X, Ding Y, Feng J, Bao X. *ACS Catal*, 2019, 9: 960–966
91 Kirilin AV, Dewilde JF, Santos V, Chojecki A, Scieranka K, Malek A. *Ind Eng Chem Res*, 2017, 56: 13392–13401
92 Chang C. *J Catal*, 1984, 90: 84–87
93 Comelli RA, Fígoli NS. *React Kinet Catal Lett*, 1994, 52: 139–147
94 Peltier FL, Chaumette P, Saussey J, Bettahar MM, Lavalley JC. *J Mol Catal A-Chem*, 1997, 122: 131–139
95 Le Peltier F, Chaumette P, Saussey J, Bettahar MM, Lavalley JC. *J Mol Catal A-Chem*, 1998, 132: 91–100
96 Wang M, Zheng L, Wang G, Cui J, Guan GL, Miao YT, Wu JF, Gao P, Yang F, Ling Y, Luo X, Zhang Q, Fu G, Cheng K, Wang Y. *J Am Chem Soc*, 2024, 146: 14528–14538
97 Tada S, Kinoshita H, Ochiai N, Chokkalingam A, Hu P, Yamauchi N, Kobayashi Y, Iyoki K. *Int J Hydrogen Energy*, 2021, 46: 36721–36730
98 Jiang Q, Lan D, Zhao G, Xu H, Gong X, Liu J, Shi Y, Zhang L, Fang H, Cheng D, Ge J, Xu Z, Liu J. *ACS Catal*, 2022, 12: 5894–5902
99 Tian P, Zhan G, Tian J, Tan KB, Guo M, Han Y, Fu T, Huang J, Li Q. *Appl Catal B-Environ*, 2022, 315: 121572
100 Zhang L, Cao Z, Gao Z, Liu W, Mao Y, Li M, Peng H. *Ind Eng Chem Res*, 2023, 62: 9123–9133
101 Wang G, Wang Y, Cao J, Wang X, Yi Y, Liu F. *Microporous Mesoporous Mater*, 2020, 291: 109693
102 Wang Q, Zheng H, Xiao D, Ren Y, Tang J. *J Mater Sci*, 2024, 59: 2315–2327
103 Chen S, Wang J, Feng Z, Jiang Y, Hu H, Qu Y, Tang S, Li Z, Liu J, Wang J, Li C. *Angew Chem Int Ed*, 2024, 63: e202316874
104 Li Z, Qu Y, Wang J, Liu H, Li M, Miao S, Li C. *Joule*, 2019, 3: 570–583
105 Li W, Zhan G, Liu X, Yue Y, Tan KB, Wang J, Huang J, Li Q. *Appl Catal B-Environ*, 2023, 330: 122575
106 Wang T, Yang C, Gao P, Zhou S, Li S, Wang H, Sun Y. *Appl Catal B-Environ*, 2021, 286: 119929
107 Tian H, Jiao J, Zha F, Guo X, Tang X, Chang Y, Chen H. *Catal Sci Technol*, 2022, 12: 799–811
108 Tian H, He H, Gao P, Guo X, Tang X, Chang Y, Zha F, Chen H. *Appl Surf Sci*, 2023, 608: 155158
109 Qu Y, Li Z, Hu H, Chen S, Wang J, Li C. *Chem Commun*, 2023, 59: 7607–7610
110 Li D, Lu X, Kinoshita H, Takemoto M, Chokkalingam A, Tada S, Iyoki K. *ACS Eng Au*, 2023, 3: 316–325
111 Harada S, Li D, Iyoki K, Ogura M. *Appl Catal A-Gen*, 2024, 669: 119517
112 Hu H, Qu Y, Feng Z, Chen S, Xu T, Wang H, Wang J, Li C. *Appl Catal A-Gen*, 2023, 666: 119410
113 Zhou C, Shi J, Zhou W, Cheng K, Zhang Q, Kang J, Wang Y. *ACS Catal*, 2020, 10: 302–310
114 Zhang X, Zhang A, Jiang X, Zhu J, Liu J, Li J, Zhang G, Song C, Guo X. *J CO2 Utilization*, 2019, 29: 140–145
115 Li W, Wang K, Zhan G, Huang J, Li Q. *ACS Sustain Chem Eng*, 2021, 9: 6446–6458
116 Xin Q, Guo H, Wang Y, Xiao L, Wang W, Wu W. *J Environ Chem Eng*, 2022, 10: 108032
117 Wang Y, Liu S, Wang J, Liu F, Ma J, Yao M, Geng S, Cao J, Li Z. *Fuel*, 2024, 357: 129727
118 Song C. *Catal Today*, 2006, 115: 2–32
119 Sakakura T, Choi JC, Yasuda H. *Chem Rev*, 2007, 107: 2365–2387
120 Benson EE, Kubiak CP, Sathrum AJ, Smieja JM. *Chem Soc Rev*, 2009, 38: 89–99
121 Wang W, Wang S, Ma X, Gong J. *Chem Soc Rev*, 2011, 40: 3703
122 Xie J, Olsbye U. *Chem Rev*, 2023, 123: 11775–11816
123 Song H, Laudenschleger D, Carey JJ, Ruland H, Nolan M, Muhler M. *ACS Catal*, 2017, 7: 7610–7622

124 Errani E, Trifiro F, Vaccari A, Richter M, Del Piero G. *Catal Lett*, 1989, 3: 65–72
125 Bradford MCJ, Konduru MV, Fuentes DX. *Fuel Processing Tech*, 2003, 83: 11–25
126 Chen Y, Han S, Pan X, Jiao F, Liu W, Pan Y, Bao X. *J Am Chem Soc*, 2024, 146: 1887–1893
127 Ma S, Huang SD, Liu ZP. *Nat Catal*, 2019, 2: 671–677
128 Fu X, Xiao J. *J Phys Chem C*, 2021, 125: 24902–24914
129 Lai Z, Sun N, Jin J, Chen J, Wang H, Hu P. *ACS Catal*, 2021, 11: 12977–12988
130 Luo J, Liu JX, Li WX. *J Phys Chem C*, 2022, 126: 9059–9068
131 Huang W, Cai J, Hu J, Zhu J, Yang F, Bao X. *Chin J Catal*, 2021, 42: 971–979
132 Tian S, Ding S, Yang Q, Ren H, Ma Q, Zhao Y, Miao Z. *RSC Adv*, 2017, 7: 20135–20145
133 Tian S, Wu Y, Ren H, Xie H, Zhao Y, Ma Q, Miao Z, Tan Y. *Fuel Processing Tech*, 2019, 193: 53–62
134 Sampath SK, Cordaro JF. *J Am Ceramic Soc*, 1998, 81: 649–654
135 Chinchen GC, Denny PJ, Jennings JR, Spencer MS, Waugh KC. *Appl Catal*, 1988, 36: 1–65
136 Hu WD, Wang CM, Wang YD, Ke J, Yang G, Du YJ, Yang WM. *Appl Surf Sci*, 2021, 569: 151064
137 Han Q, Gao P, Chen K, Liang L, Zhao Z, Yao X, Xiao D, Han X, Hou G. *Chem*, 2023, 9: 721–738
138 Zhang X, Zhang G, Liu W, Yuan F, Wang J, Zhu J, Jiang X, Zhang A, Ding F, Song C, Guo X. *Appl Catal B-Environ*, 2021, 284: 119700
139 Cheng K, Zhou W, Kang J, He S, Shi S, Zhang Q, Pan Y, Wen W, Wang Y. *Chem*, 2017, 3: 334–347
140 Fujiwara K, Akutsu T, Nishijima M, Tada S. *Top Catal*, 2023, 66: 1492–1502
141 Lee K, Dickieson MP, Jung M, Yang Y, Yan N. *ACS Catal*, 2024, 14: 3074–3089
142 Aghabeygi S, Khademi-Shamami M. *Ultrasons SonoChem*, 2018, 41: 458–465
143 Wang C, Garbarino G, Allard LF, Wilson F, Busca G, Flytzani-Stephanopoulos M. *ACS Catal*, 2016, 6: 210–218
144 Pinheiro Araújo T, Morales-Vidal J, Zou T, Agrachev M, Verstraeten S, Willi PO, Grass RN, Jeschke G, Mitchell S, López N, Pérez-Ramírez J. *Adv Energy Mater*, 2023, 13: 2204122
145 Ding J, Li Z, Xiong W, Zhang Y, Ye A, Huang W. *Appl Surf Sci*, 2022, 587: 152884
146 Feng Z, Tang C, Zhang P, Li K, Li G, Wang J, Feng Z, Li C. *J Am Chem Soc*, 2023, 145: 12663–12672
147 Han S, Zhao D, Otroshchenko T, Lund H, Bentrup U, Kondratenko VA, Rockstroh N, Bartling S, Doronkin DE, Grunwaldt JD, Rodemerck U, Linke D, Gao M, Jiang G, Kondratenko EV. *ACS Catal*, 2020, 10: 8933–8949
148 Tada S, Ochiai N, Kinoshita H, Yoshida M, Shimada N, Joutsuka T, Nishijima M, Honma T, Yamauchi N, Kobayashi Y, Iyoki K. *ACS Catal*, 2022, 12: 7748–7759
149 Redekop EA, Cordero-Lanzac T, Salusso D, Pokle A, Oien-Odegaard S, Sunding MF, Diplas S, Negri C, Borfecchia E, Bordiga S, Olsbye U. *Chem Mater*, 2023, 35: 10434–10445
150 Nikolajsen MT, Grivel JC, Gaur A, Hansen LP, Baumgarten L, Schjødt NC, Mentzel UV, Grunwaldt JD, Sehested J, Christensen JM, Høj M. *J Catal*, 2024, 431: 115389
151 Chen S, Ma S, Liu ZP. *J Phys Chem Lett*, 2021, 12: 3328–3334
152 Zhang J, An B, Li Z, Cao Y, Dai Y, Wang W, Zeng L, Lin W, Wang C. *J Am Chem Soc*, 2021, 143: 8829–8837
153 Lin L, Wang G, Zhao F. *ChemistrySelect*, 2021, 6: 2119–2125
154 Zhou S, Li S. *J Phys Chem C*, 2020, 124: 27467–27478
155 Ling Y, Luo J, Ran Y, Liu Z, Li WX, Yang F. *J Am Chem Soc*, 2023, 145: 22697–22707
156 Ye A, Li Z, Ding J, Xiong W, Huang W. *ACS Catal*, 2021, 11: 10014–10019
157 Zhao YF, Rousseau R, Li J, Mei D. *J Phys Chem C*, 2012, 116: 15952–15961
158 Davis R, Walsh JF, Muryn CA, Thornton G, Dhanak VR, Prince KC. *Surf Sci*, 1993, 298: L196–L202
159 Wang Y, Kováčik R, Meyer B, Kotsis K, Stodt D, Staemmler V, Qiu H, Traeger F, Langenberg D, Muhler M, Wöll C. *Angew Chem Int Ed*, 2007, 46: 5624–5627
160 Medford AJ, Sehested J, Rossmeisl J, Chorkendorff I, Studt F, Nørskov JK, Moses PG. *J Catal*, 2014, 309: 397–407
161 Su J, Wang D, Wang Y, Zhou H, Liu C, Liu S, Wang C, Yang W, Xie Z, He M. *ChemCatChem*, 2018, 10: 1536–1541
162 Fu X, Li J, Long J, Guo C, Xiao J. *ACS Catal*, 2021, 11: 12264–12273